Grains3D, a flexible DEM approach for particles of arbitrary convex shape-Part III: extension to non-convex particles modelled as glued convex particles

Andriarimina Daniel Rakotonirina, Jean-Yves Delenne, Farhang Radjai, Anthony Wachs

Grains3D, a flexible DEM approach for particles of arbitrary convex shape - Part III: extension to non convex particles modeled as glued convex particles

Andriarimina Daniel Rakotonirina · Jean-Yves
Delenne · Farhang Radjai · Anthony Wachs

Abstract Large-scale numerical simulation using the Discrete Element Method (DEM) contributes to improve our understanding of granular flow dynamics involved in many industrial processes and geophysical flows. In industry, it leads to an enhanced design and an overall optimisation of the corresponding equipment and process. Most of DEM simulations in the literature have been performed using spherical particles. A limited number of studies dealt with non-spherical particles, even less with non-convex particles. Even convex bodies do not always represent the real shape of certain particles. In fact, more complex shaped particles are found in many industrial applications as, e.g., catalytic pellets in chemical reactors or crushed glass debris in recycling processes. In Grains3D-Part I [39], we addressed the problem of convex shape in granular simulations while in Grains3D-Part II [33], we suggested a simple through efficient parallel strategy to compute systems with up to a few hundreds of millions of particles. The aim of the present study is to extend even further the modeling capabilities of Grains3D towards non-convex shapes, as a tool to examine the flow dynamics of granular media made of non-convex particles. Our strategy is based on decomposing a non-convex shaped particle into a set of convex bodies, called elementary components. We call our method *glued* or *clumped convex* method, as an extension of the popular *glued spheres* method. Essentially, a non-convex particle is constructed as a cluster of convex particles, called elementary components. At the level of these elementary components of a glued convex particle, we employ the same contact detection strategy based on a Gilbert-Johnson-Keerthi algorithm and a linked-cell spatial sorting that accelerates the resolution of the contact, that we introduced in [39]. Our *glued convex* model is implemented as a new module of our code Grains3D and is therefore automatically fully parallel. We illustrate the new modeling capabilities of Grains3D in two test cases: (i) the filling of a container and (ii) the flow dynamics in a rotating drum.

Keywords Granular flow · Discrete Element Method · non convex shape · GJK algorithm · Glued convex

Andriarimina Daniel Rakotonirina
IFP Energies nouvelles, Fluid Mechanics Department, Rond-point de l'Echangeur de Solaize, BP 3, 69360 Solaize, France

Andriarimina Daniel Rakotonirina · Anthony Wachs
Department of Mathematics, 1984 Mathematics Road, Vancouver, BC, V6T 1Z4, Canada

Anthony Wachs
Department of Chemical & Biological Engineering, University of British Columbia, 2360 East Mall, Vancouver, BC, V6T 1Z3, Canada,
E-mail: wachs@math.ubc.ca

Jean-Yves Delenne
IATE, UMR 1208 INRA – CIRAD – Montpellier Supagro – Université Montpellier 2, 2 place Pierre Viala, 34060 CEDEX, Montpellier, France

Farhang Radjai
University Montpellier 2, CNRS, LMGC UMR 5508, Place Eugène Bataillon, F-34095 Montpellier Cedex, France

Farhang Radjai
MultiScale Material Science for Energy and Environment, UMI 3466 CNRS-MIT, DCEE, Massachusetts Institute of Technology, 77 Massachusetts Avenue, Cambridge, CA 02139, USA

1 Introduction

Discrete Element Method was originally designed to handle spherical particles [6]. The method is now able to deal with more complex particle shapes [7,14,39]. Thanks to its conceptual simplicity this method is widely used in granular media modelling. Its computational implementation is very straightforward for spheres but is quite difficult for complex particle shapes. Many approaches have been investigated since the late 80's, among them the works of Cundall [7] and Hart [14]. They studied a system composed of polyhedral blocks and used a robust and rapid technique (Common Plane technique) to detect and to categorise contacts between two polyhedral blocks. Later on, various authors worked on the extension of DEM to non-spherical particles. Li *et al.* [24] modelled sphero-disc particles to study the flow behaviour, the arching and the discharging in a hopper. Another extension of Discrete Element Method to polygonal shaped particles was suggested by Feng and Owe [10] and to polyhedral shaped particles by Fraige *et al.* and Lee *et al.* [11,23]. These new features enabled research groups to address several problems in the field of geophysics [4,18, 15]. Munjiza *et al.* [28] constructed a poly-ellipsoid particle by "gluing" ellipsoids together. One of the most famous extensions of DEM is the "glued spheres" model in which a complex shape is approximated by "gluing" spherical particles. For instance, Nolan and Kavanagh [29] used a glued spheres model to study the random close packings of cylindrical-, bean- and nail-shaped particles. They found good agreement between their simulation results and available experimental data. Song *et al.* [35] also used a glued spheres model to study tablet-flat wall and tablet-tablet contacts. At first sight, this method seems to be well adapted to any shape. Nonetheless, the higher the number of spheres is, the less efficient the computation becomes, as Song *et al.* [35] demonstrated. In addition, the glued spheres approximation introduces an articifial roughness at the particle boundary [16] that varies with the size and the number of spheres. Although the "glued spheres" model is a coarse geometric representation of a complex shape, it is still widely employed nowadays, even for rather simple non-spherical convex shapes for which a more advanced (in the sense angularity or shape preserving) modeling approach could have easily been used as, e.g., [42] for cubes, [36] for cylinders and [45] for tetrahedra.

Available strategies in the literature to handle complex shapes were already reviewed in detail in Grains3D-Part I [39] and comprehensively summarized by Lu *et al.* in [25]. We simply give here again a short (and incomplete) overview. Williams and O'Connor [40] introduced the Discrete Function Representation (DFR) of a particle shape to address contact resolution. DFR is applicable to convex shapes and to a restricted set of concave shapes. Williams and Pentland [41] explored the critical influence of particle shape on granular dynamics and suggested super-quadric particles for geophysical applications. This method allows the design of particles with rounded edges such as ellipsoid, rounded blocks, or rounded tablets by introducing a continuous function $f(x, y, z) = (x/a)^m + (y/b)^n + (z/c)^p - 1 = 0$ that defines the body shape. The weakness of this method relies on the handling of contact detection. In fact, as edge angularity increases, more discretisation points are required to represent $f(x, y, z)$ locally at the contact point. Therefore, the computing cost associated to contact detection increases with edge (or shape) angularity. A probability-based contact algorithm is presented in the work of Jin *et al.* [17]: contacts between non-spherical particles are recast into those between spherical particles with probability. Alonso-Marroquín and Wang [2] presented a method to simulate two-dimensional granular materials with sphero-polygon shaped particles. The particle shape is represented by the classical concept of a Minkowski sum [3], which permits the representation of complex shapes without the need to define the object as a composite of spherical or convex particles. Hence, this approach has proven to be much better than the glued spheres method. The modelling of non-spherical particles using the so-called generalized "sphero-simplices" has received a particular interest over the last decade [2,32]. A *spherosimplex*-shaped particle is combination of a skeleton (e.g. a point, a linear segment, a polygon or a polyhedron) and a disk or a sphere. The use of Minkowski sums is also a primary feature of our own contact detection method [39].

The literature on numerical models for particles of non-convex shape is rather scarce. In theory, the "glued spheres" model can represent any shape, including non-convex shapes, but the model has shown limited accuracy even for simple shapes as a cylinder [19]. The *spherosimplex* representation is able to handle non-convex shapes with rounded corners/edges (as the skeleton is spanned by a disk or a sphere). The ultimate solution, that might be inefficient from a computational viewpoint as the collision detection step is certainly very time consuming, involves meshing the surface of the non-convex bodies, as attempted by Remond *et al.* [34]. The method in [34] produced spectacular

results on the packing of crushed hollow cylinders, but (serial) computations were limited to 10,000 particles maximum.

Contact resolution is a core component of DEM simulations. A proper contact resolution ensures accurate DEM computed solutions. When combined with pre and post homotheties applied to two presumably colliding bodies, the Gilbert-Johnson-Keerthi (GJK) algorithm [37,13] is a good candidate for this particular problem and well suited for arbitrary convex shaped particles. The GJK-based strategy was first introduced by Petit *et al.* in 2001 [31] and later generalized in Grains3D-Part I by Wachs *et al.* [39] to study the effect of non-spherical particle shape in granular flows. The GJK algorithm is an iterative approach to compute the minimal Euclidean distance between two convex bodies. The GJK reduces the problem of finding the minimal distance between two convex bodies to finding the minimal distance between their Minkowski difference and the origin [13].

Beyond the problem of contact detection, modelling difficulties related to multiple contact handling for complex shaped particles also require to be addressed. In the existing literature on this problem, Abbaspour-Fard [1] employed a multi-sphere model to examine various phenomena such as sliding, dropping and conveying, while Kruggel-Emden *et al.* [20] studied the macroscopic collision properties of the glued sphere model and compared them to experimental data. In their study, the total contact force of a multi-sphere particle impacting a flat wall is treated by computing the mean of the forces at each contact point. Later on Höhner *et al.* [16] pointed out that this method may not be accurate enough. They showed that there is a non-negligible effect of the particle shape approximation (artificial roughness created by glueing spheres) on the force temporal evolution in normal and tangential directions.

Our main objective is to elaborate on the construction of a simple glued/clumped convex method to model non-convex shapes. Our method is based on existing and validated tools already introduced in the two first chapters of this trilogy of papers on Grains3D [39,33]. Our method shares some features with the method used in the Bullet Physics library [5], developed for video games, virtual reality and movies, to handle contacts between convex and non-convex bodies. The rest of the paper is organized as follows. In *Section 2*, we shortly explain how the method works conceptually and how we address the problem of multiple contact points. We present in *Section 3* two validation cases, the former involving the impact of a convex body decomposed into a set of smaller convex bodies on a flat wall and the latter involving a comparison against experimental data in a far more complex flow configuration. *Section 4* illustrates further the modeling capabilities of the new non-convex module of Grains3D. Unprecedented simulation results on the packing and the flow of 2D/3D cross-like particles are shown. Concluding remarks and perspectives are given in *Section 5*.

2 The glued convex method

The glued convex method is a simple though powerful idea. It is based on decomposing a non-convex particle, called the composite, into a set of convex bodies, called elementary components, as illustrated in 2D in FIG. 1. It can hence be seen as an extension or a generalization of the glued spheres method introduced by [29]. However, contrary to the glued spheres method, our glued convex method keeps:

(i) the original angularity of the non-convex shape,
(ii) the particle surface smooth and does not introduce any artificial roughness.

These two features are deemed to be major improvements with respect to the glued spheres method. Our glued convex method is implemented in our in-house granular solver Grains3D [39]. This enable us to use existing methods, models and algorithms already implemented in Grains3D such as time integration of equations of motion, quaternions/matrices for body rotation, linked-cell spatial sorting and the Gilbert-Johnson-Keerthi algorithm for collision detection [13,12]. In particular, the GJK algorithm is applied to the elementary components. A contact between a glued convex particle, i.e., a composite, and another glued convex particle, i.e., another composite, is detected if at least one elementary component of the former contacts with one elementary component of the latter.

2.1 Equations of motion

The dynamics of a granular material made of (non-convex) particles is entirely governed by Newton's law. Assuming that the granular system is made of N particles, each particle $i \in\ <0, N-1>$ satisfies the following set of governing equations:

$$M_i \frac{d\mathbf{U_i}}{dt} = \mathbf{F_i} \quad , \quad \mathbf{J_i}\frac{d\boldsymbol{\omega}_i}{dt} + \boldsymbol{\omega}_i \wedge \mathbf{J_i}\boldsymbol{\omega}_i = \mathbf{M_i} \tag{1}$$

$$\frac{d\mathbf{x_i}}{dt} = \mathbf{U_i} \quad , \quad \frac{d\boldsymbol{\theta}_i}{dt} = \boldsymbol{\omega}_i \tag{2}$$

where M_i, $\mathbf{J_i}$, $\mathbf{x_i}$ and $\boldsymbol{\theta}_i$ denote the mass, moment of inertia tensor, position of the centre of mass and angular position of particle i, $i \in [0, N-1]$. The translational velocity vector $\mathbf{U_i}$ and the angular velocity vector $\boldsymbol{\omega}_i$ of the centre of mass are involved in the decomposition of the velocity vector as $\mathbf{v_i} = \mathbf{U_i} + \boldsymbol{\omega}_i \wedge \mathbf{R_i}$, where $\mathbf{R_i}$ denotes the position vector with respect to the centre of mass of a particle i. As in [39], the angular position is actually tracked by a quaternion or equivalently by a rotation matrix with respect to the initial (reference) angular position. For the easiness of presentation, we use a rotation matrix later on and denote it $\mathcal{M}_i$. $\mathbf{F_i}$ and $\mathbf{M_i}$ stand for the sum of all forces and torques applied to particle i. They are defined as follows:

$$\mathbf{F}_i = M_i \mathbf{g} + \sum_{j=0, j\neq i}^{N-1} \mathbf{F}_{ij} \tag{3}$$

$$\mathbf{M}_i = \sum_{j=0, j\neq i}^{N-1} \mathbf{R}_j \wedge \mathbf{F}_{ij} \tag{4}$$

$\mathbf{R}_j$ denotes a vector which points from the centre of mass of the particle i to the contact point with particle j. It is assumed in this work that all particles are subjected to gravity and contact forces only, although additional forces and torques can be easily added, provided appropriate corresponding physical models are available, as cohesive, electrostatic, hydrodynamic, etc.

2.2 Solution strategy for composite particles

At each discrete time and for each composite particle i made of K elementary convex components $k \in\ <0, K-1>$, we perform the following steps :

1. detect contact points with surrounding composite particles by detecting contact points between elementary convex components $k \in\ <0, K-1>$ of composite i and elementary convex components of surrounding composites,
2. compute contact forces and contact torques. Torques must be computed with the right leverage, i.e. the vector from the center of mass of composite i and the point of contact, and not from the center of mass of the elementary component k,
3. solve the time-discretized form of Eq. (1)-Eq. (2) to supply the new velocity $(\mathbf{U}_i, \boldsymbol{\omega}_i)$ and position $(\mathbf{x}_i, \mathcal{M}_i)$ of composite particle i,
4. update the velocity $(\mathbf{U}_{k,i}, \boldsymbol{\omega}_{k,i})$ and position $(\mathbf{x}_{k,i}, \mathcal{M}_{k,i})$ of its elementary components using standard kinematic relations.

These standard kinematic relations read as follows. Assuming $\mathbf{x}_i^0$ denotes the initial position of composite i, $\mathbf{x}_{k,i}^0$ the initial position of elementary component k of composite i and $\mathbf{r}_{k,i}^0 = \mathbf{x}_{k,i}^0 - \mathbf{x}_i^0$ the initial leverage of elementary component k, we have for each elementary component k of composite i:

$$\boldsymbol{\omega}_{k,i} = \boldsymbol{\omega}_i \quad , \quad \mathcal{M}_{k,i} = \mathcal{M}_i \tag{5}$$

$$\mathbf{U}_{k,i} = \mathbf{U}_i + \boldsymbol{\omega}_{k,i} \wedge (\mathcal{M}_{k,i} \cdot \mathbf{r}_{k,i}^0) \quad , \quad \mathbf{x}_{k,i} = \mathbf{x}_i + (\mathcal{M}_{k,i} \cdot \mathbf{r}_{k,i}^0) - \mathbf{r}_{k,i}^0 \tag{6}$$

2.3 Mass properties

One of the challenges encountered with a non-convex particle shape is the computation of its mass properties (volume, centre of mass and components of moment of inertia tensor). In fact, the numerical integration of the different volume sums theoretically involves the use of sophisticated geometric intersection operations often referred to as Boolean Algebra on rigid bodies since our non-convex particles are made of arbitrary convex elementary components that can overlap (and most of the time do overlap). This can be achieved by resorting to using an appropriate library such as the Computational Geometry Algorithms Library [8]. We opt for an alternative computing method that is simple to implement but nonetheless provides an accurate approximation of the various volume sums corresponding to the particle mass properties. Our in-house method basically involves pixelating the particle and shares similarities with the method suggested by Alonso-Marroquín and Wang [2] except that the set of points we use to compute the volume sums are located on a structured lattice while Alonso-Marroquin and Wang use an actual Monte-Carlo method with quasi-random distribution of points inside the non-convex body. We compared our structured lattice method to Monte-Carlo random distribution of points and did not find that the Monte-Carlo method is significantly faster and/or actually even just faster for the same level of accuracy, depending on the body shape. Our structured lattice method unfolds as follows:
 – define a box that embeds the body (FIG. 2),
 – uniformly discretise the box in the three directions to create a three-dimensional mesh of constant grid size,
 – find which cell centers $\mathbf{X}$ are inside the body,
 – sum up contributions of cells tagged inside to approximate the volume sum.
Volume sums are hence approximated in the following way:

$$\int_V f(\boldsymbol{x})d\boldsymbol{x} \simeq \sum_{l=0}^{N_x-1} \sum_{m=0}^{N_y-1} \sum_{n=0}^{N_z-1} f(\mathbf{X}_{lmn})\phi(\mathbf{X}_{lmn})v_{lmn} \tag{7}$$

where N_x, N_y and N_z denote the numbers of cells in each direction, $\phi(\mathbf{X})$ is a binary indicator function that equals 1 when $\mathbf{X}$ is inside the particle and 0 otherwise, v_{lmn} denotes the volume of cell lmn (actually $v_{lmn} = v_{cell} = constant$ as the mesh has a constant grid size) and f is a scalar or vector-valued function that takes the following forms:
 – $f = 1$ to compute the particle volume,
 – $f = \mathbf{X}$ to compute the position $\mathbf{X}_g$ of the centre of mass as:

$$\mathbf{X}_g \simeq \frac{1}{V} \sum_{l=0}^{N_x-1} \sum_{m=0}^{N_y-1} \sum_{n=0}^{N_z-1} \mathbf{X}_{lmn}\phi(\mathbf{X}_{lmn})v_{cell} \tag{8}$$

 – $f = X_y^2 + X_z^2$, $f = X_x^2 + X_z^2$, $f = X_x^2 + X_y^2$, $f = -X_x X_y$, $f = -X_y X_z$ and $f = -X_x X_z$ to compute J_{xx}, J_{yy}, J_{zz}, $J_{xy} = J_{yx}$, $J_{yz} = J_{zy}$ and $J_{xz} = J_{zx}$, respectively.
 We illustrate in FIG. 3 the spatial convergence properties of our algorithm applied to the calculation of the volume (FIG. 3(a)) and the components of the moment of inertia tensor (FIG. 3(b)) of a sphere, a cylinder and two overlapping cylinders. The relative error between the approximated volume and the true volume is plotted as a function of the number of discretisation points per direction. The error decreases in a slightly non-monotone but overall linear way as the number of discretisation points per direction increases. From 500 points, the error on both the volume and the components of the moment of inertia tensor is less than 0.2% for the three shapes considered. In this study, all computations of mass properties of glued convex particles are performed with at least $1,000$ discretisation points per direction to ensure a satisfactory level of accuracy (Nota: N_x, N_y and N_z are not necessarily equal is the particle aspect ratio is larger than 1). For the sake of completeness, we point out that $1,000$ points per direction translates into $1,000,000,000$ cells and hence $K \times 1,000,000,000$ in/out tests, which might correspond to a lot of such geometric tests, performed with the GJK algorithm, and hence a significant computing time. This impression is however biased for two reasons: (i) our algorithm is parallelized by standard domain decomposition and distributed computing hence markedly speeds up computations (with literally zero communication overhead as a simple MPI_Gather on the master process is sufficient to sum all contributions coming from the different processes), and (ii) these properties are computed once and for all for a certain shape and are then stored in a shape database to be later uploaded for

actual granular simulations. To get an order of magnitude, the computation of the mass properties of a composite particle made of 5 elementary convex components on a $1,000^3$ mesh takes less than 5 minutes on 64 cores.

2.4 Time integration

As suggested in Grains3D-Part I [39], Eq. (1)-Eq. (2) are integrated in time with a second-order leap-frog Verlet scheme. For the sake of completeness, we shortly recall below how the leap-frog Verlet scheme ([21,22]) is constructed for the translational motion (the same applies to the angular motion):

$$
\begin{aligned}
\mathbf{U}\left(t + \frac{\Delta t}{2}\right) &= \mathbf{U}\left(t - \frac{\Delta t}{2}\right) + \frac{\mathbf{F}(t)}{M}\Delta t \\
\mathbf{x}(t + \Delta t) &= \mathbf{x}(t) + \mathbf{U}\left(t + \frac{\Delta t}{2}\right)\Delta t
\end{aligned}
\tag{9}
$$

As pointed out in [9] and elsewhere, at least a second-order accurate in time scheme is required to properly predict the time evolution of a granular system.

2.5 GJK-based contact detection for non-convex particles

In Grains3D-Part I [39], we elaborated on a contact detection method for arbitrary convex bodies based on a GJK algorithm. Introduced by [13], the GJK algorithm originally computes the minimal distance between two convex polyhedra. In 1990, the algorithm was improved by Gilbert and Foo [12] to deal with general convex bodies. Since in our method each elementary component of a non-convex particle is a convex body, we can readily apply the GJK algorithm to each elementary component to detect a potential collision with other elementary components of a neighbouring non-convex particle.

As pointed out in Grains3D-Part I [39], the GJK algorithm applied right away to convex bodies is helpful to determine whether two convex bodies touch or not (if they do touch, the minimal distance between them is 0) but does not supply information on the contact features as contact point, overlap distance and unit normal vector at the point of contact. To access this information, we suggested in Grains3D-Part I [39] a 3-step procedure that consists of a sequence of (1) slightly shrinking the bodies such that they do not overlap anymore, (2) using the GJK algorithm to compute the minimal distance, and (3) swelling back the bodies to their original size and reconstructing contact features. For further details on our contact detection method for arbitrary convex shaped particles, the interested reader is referred to [39].

Proximity queries are performed with spheres circumscribed to non-convex particles and a linked-cells spatial sorting. Our linked-cells spatial sorting is based on non-convex composite particles and hence the size of cells is greater or equal to the diameter of the largest sphere circumscribed to the non-convex particles. Potential contacts of a particle with its neighboring particles are computed by looping over particles that belong to cells that are neighbors to the cell the particle belongs to. Once this list of neighboring particles is established, it is further narrowed down by testing the potential overlap of corresponding circumscribed spheres. For standard convex particles, we would apply our 3-step GJK-based contact detection method to these pairs of particles and determine which pairs actually contact. For non-convex particles, we need to loop over the elementary components and apply the sequence (i) proximity queries based on spheres circumscribed to the elementary components of each non-convex particle and (ii) if positive, contact detection method for these pairs of elementary components. The whole contact detection strategy for non-convex particles has hence a 2-level nested loop structure. For proximity queries, we use spheres circumscribed to non-convex particles in the outer loop and spheres circumscribed to their elementary convex components in the inner loop. The method reads as follows:

1. Use linked-cells to find pairs of particles (P_i, P_j) that potentially touch,
2. Narrow down this list by determining pairs of particles (P_i, P_j) whose circumscribed spheres overlap,
3. For each of this pair, loop over elementary components E_k of composite particle P_i. For each E_k, loop over elementary components E_l of composite particle P_j to determine which pairs (E_k, E_l) have overlapping circumscribed spheres and hence potentially touch,

4. For each of these pairs (E_k, E_l), apply the 3-step GJK-based contact detection method to determine which pairs actually touch and compute contact point features.

The contact detection method for two non-convex particles theoretically scales as $N_i \times N_j$ where N_i and N_j are the number of elementary components of particle P_i and the number of elementary components of particle P_j, respectively. This could be seen as the main drawback of our method, which results into a significant increase of the computing time for a granular system made of non-convex particles with respect to a granular system made of convex particles. In practice, the ratio between non-convex and convex is more of the order of $\alpha N_i N_j$, with $\alpha \in \,]0:1]$. The inner loop of proximity queries normally limits the number of calls to the 3-step GJK-based contact detection method for elementary components, but this strongly depends on the shape itself, and any general estimate is very hard to supply. Actually, we can establish a hierarchy of computing time between spheres, convex bodies and non-convex bodies. Spheres contact detection is analytical, convex bodies contact detection requires one call to our 3-step GJK-based contact detection method and non-convex bodies contact detection requires several calls to our 3-step GJK-based contact detection method. For the sake of illustration, although the following numbers should be considered with great care are they are strongly shape dependent, we can roughly state that for the same flow configuration, a computation with convex bodies (let's say cubes, for instance) is $\sim$ 5-fold more time-consuming than with spheres, and the same computation with non-convex bodies is itself $\sim$ 5- to 10-fold more time-consuming than with convex bodies, so about 50-fold more time-consuming than with spheres. The computing cost is high, but we claim that this is the price to pay to accurately represent a non-convex shape. Interestingly, and as pointed in Grains-Part II [33], since contact detection is a serial operation and its cost for non-convex bodies is markedly larger than spheres or convex bodies, parallel computations of granular systems made of non-convex particles scales extremely well (with a weak scaling factor close to 1). In fact, the MPI communication overhead is literally negligible compared to the contact detection phase per sub-domain, i.e., per process.

2.6 Contact force and torque model

For all simulations performed in this work, we use the same contact force model as in Grains3D-Part I [39]. It is a simple Hookean spring-dashpot-Coulomb frictional slider model. The total contact force $\mathbf{F}_{ij,l}$ between two particles i and j at contact point l reads as follows:

$$\mathbf{F}_{ij,l} = \mathbf{F}_{ij,l,el} + \mathbf{F}_{ij,l,dn} + \mathbf{F}_{ij,l,t} \tag{10}$$

where $\mathbf{F}_{ij,l,el} = k_n \delta_{ij,l} \mathbf{n}_c$ is the Hookean normal elastic force, $\mathbf{F}_{ij,l,dn} = -2\gamma_n m_{ij} \mathbf{U}_{rn}$ is the normal dissipative force and $\mathbf{F}_{ij,l,t} = -\min\{\mu_c|\mathbf{F}_{ij,l,el} + \mathbf{F}_{ij,l,dn}|, |-2\gamma_t m_{ij}\mathbf{U}_{rt} - k_s \int_{t_s}^t \mathbf{U}_{rt}dt|\}\mathbf{t}_c$ is the tangential Coulomb force. k_n denotes the normal contact stiffness, $\delta_{ij,l}$ the overlap distance, $\mathbf{n}_c$ the unit normal vector at contact point, γ_n the normal dissipative coefficient, m_{ij} the reduced mass, $\mathbf{U}_{rn}$ the normal relative velocity at contact point, μ_c the Coulomb tangential friction coefficient, γ_t the dissipative tangential friction coefficient, $\mathbf{U}_{tn}$ the tangential relative velocity at contact point, k_s the static tangential friction coefficient and t_s the time at which contact started. For more detail and meaning of parameters, the interested reader is referred to [38,39]. As in [38,39], the influence of the term $-k_s \int_{t_s}^t \mathbf{U}_{rt}dt$ has been found to be very limited in the granular configurations investigated, even in quasi-static configurations as a packing. If γ_t is chosen sufficiently large, results with $k_s = 0$ and $k_s \neq 0$ are almost indistinguishable. In fact, a small residual velocity $\mathbf{U}_{rt}$ (inevitable in DEM computations as a result of the explicit integration in time of the momentum equation of particles involved in multiple simultaneous contacts) is enough for the tangential force $\mathbf{F}_{ij,l,t}$ to saturate to $\mu_c|\mathbf{F}_{ij,l,el} + \mathbf{F}_{ij,l,dn}|\mathbf{t}_c \simeq \mu_c|\mathbf{F}_{ij,l,el}|\mathbf{t}_c$ (as $|\mathbf{F}_{ij,l,dn}| \ll |\mathbf{F}_{ij,l,el}|$ when $\mathbf{U}_{rn}$ is small). The most critical configuration is a packing in which the set of particles theoretically relaxes to full rest. With $k_s = 0$, the dynamics of the system is characterized by two time scales/stages: (i) stage 1 relevant of a short time scale over which particles are poured/inserted, settle by gravity, collide and reach a pseudo-stationary state of rest, followed by (ii) stage 2 relevant of an extremely long time scale over which the system is characterized by very slow (and non physical) creeping deformations. At the end of stage 1, simulation results with $k_s = 0$ and $k_s \neq 0$ are similar and the packing is indeed representative of a frictional system controlled by the magnitude of μ_c. Hence, we take $k_s = 0$ thereafter and analyze results for packings at the end of stage 1. Please note that this is

not a general comment on the choice of k_s. In fact, in other configurations, the above comment may not apply. Finally, we set the rolling resistance coefficient k_{ms} [39] to 0 (i.e. no rolling torque resistance) in all simulations as particles are all non-spherical in this work.

In the case of a contact between two convex particles, the number of contact points is assumed to be $N_c = 1$ and we always have $l \in< 0, N_c - 1 > \Rightarrow l = 0$. In the case of multiple contact points, i.e., $N_c > 1$, there are essentially two simple ways to compute the total contact force between two particles:

- Model A: by summing contributions from all contact points,
- Model B: by averaging contributions from all contact points over the total number of contact points N_c.

Model B is the most intuitive and actually the solution adopted by Kruggel-Emden *et al.* [20] and Höhner *et al.* [16]. In the latter work, the authors compute forces incrementally to account for the fact that the number of contact points can vary over the full duration of contact between two particles. In this work, we adopt the simple approach of Kruggel-Emden *et al.* [20]. The total contact force between two non-convex composite particles is calculating as a mean contact force over all their contact points. In other words, the total contact force is the sum of all forces resulting from contacts between two elementary components of the two non-convex composite particles divided by the total number of contact points. Same applies to the total torque where contributions of each contact point is calculated with respect to the centre of mass of the non-convex composite particle, not the center of mass of the elementary component.

Both Model A and Model B are acceptable and lead to the right restitution in a simplified normal contact. However, Model A has two drawbacks: both contact duration T_c and normal dissipative coefficient γ_n depend on N_c, while they do not for Model B. Let us shortly show this property by considering a simple normal, gravityless, frictionless normal contact between a sphere and a flat surface at a pre-collisional velocity v_0. This is a nice toy problem as we can solve it analytically. The penetration depth δ over contact duration solves a similar equation as the one introduced in Grains3D-Part I [39]:

$$\frac{d^2\delta}{dt^2} + 2\gamma_n \frac{d\delta}{dt} + \omega_0^2 \delta = 0 \,, \ \delta(t=0) = 0 \,, \ \frac{d\delta}{dt}(t=0) = v_0 \tag{11}$$

except that $\omega_0^2 = \dfrac{k_n}{M}$ for a sphere-flat wall contact (assuming the motionless flat wall, being a fixed obstacle, has an infinite mass) instead of $\omega_0^2 = \dfrac{2k_n}{M}$ for a sphere-sphere contact. As shown in [39], the solution writes $\delta(t) = \frac{v_0}{\sqrt{\omega_0^2 - \gamma_n^2}} e^{-\gamma_n t} \sin\left(\sqrt{\omega_0^2 - \gamma_n^2}\, t\right)$ and can be characterized by contact duration T_c, time of maximum overlap T_{max} and maximum penetration depth δ_{max} as follows:

$$T_c = \frac{\pi}{\sqrt{\omega_0^2 - \gamma_n^2}}, \tag{12}$$

$$T_{max} = \frac{1}{\sqrt{\omega_0^2 - \gamma_n^2}} \arctan\left(\frac{\sqrt{\omega_0^2 - \gamma_n^2}}{\gamma_n}\right), \tag{13}$$

$$\delta_{max} = \delta(t = T_{max}). \tag{14}$$

In particular, the coefficient of restitution e_n, defined as the ratio of post-collisional velocity to pre-collisional velocity, can be expressed as:

$$e_n = \left| \frac{\frac{d\delta}{dt}(t = T_c)}{v_0} \right| = e^{-\gamma_n T_c} = e^{-\gamma_n \frac{\pi}{\sqrt{\omega_0^2 - \gamma_n^2}}} \tag{15}$$

Given e_n and k_n, the normal dissipative coefficient γ_n can be deduced from EQ. (15):

$$\gamma_n = -\frac{\omega_0 \ln e_n}{\sqrt{\pi^2 + (\ln e_n)^2}} \tag{16}$$

In Model A, in which forces at each contact point are summed, it is easy to see that our toy model equation EQ. (11) becomes:

$$\frac{d^2\delta}{dt^2} + 2N_c \gamma_n \frac{d\delta}{dt} + \widetilde{\omega_0}^2 \delta = 0 \,, \ \delta(t=0) = 0 \,, \ \frac{d\delta}{dt}(t=0) = v_0 \tag{17}$$

where $\widetilde{\omega_0}^2 = N_c \dfrac{k_n}{M}$. Setting $\widetilde{\gamma_n} = N_c \gamma_n$, EQ. (17) has exactly the same form as EQ. (11). After some simple algebra, we obtain:

$$\gamma_n = -\sqrt{\frac{2k_n}{N_c M}} \frac{\ln e_n}{\sqrt{\pi^2 + (\ln e_n)^2}}, \tag{18}$$

$$T_c = \frac{\pi}{\sqrt{\widetilde{\omega_0}^2 - \widetilde{\gamma_n}^2}} \to \frac{\pi M}{N_c k_n} \text{ as } e_n \to 1 \tag{19}$$

So basically, model A has a contact duration T_c and a normal dissipative coefficient γ_n that decrease with the number of contact points, as $1/\sqrt{N_c}$ and $1/N_c$, respectively. As an illustration, we show in FIG. 5 how γ_n varies with e_n and N_c. Because forces from all contact points are summed, EQ. (18) corrects the excessive dissipation (damping) of the system with the factor $1/\sqrt{N_c}$. But the major drawback of Model A is the decrease of T_c with N_c. The higher the number of contact points between elementary components is, the shorter the contact time is. This is a very undesirable property. In fact, in a complex granular flow, it is hard to estimate a priori N_c (or max N_c over all possible contacts between non-convex composite particles in the granular flow, that would supply min T_c). The time-step magnitude Δt in a DEM simulation is generally set to a fraction of the contact duration T_c, typically $\Delta t = T_c/20$ or smaller. For model A, because T_c is hard to estimate a priori, estimating Δt to guarantee a satisfactory time evolution of the computed solution is even harder than in a DEM simulation of spherical or convex paricles in which $N_c = 1$.

In model B, the total normal force is expressed as:

$$\mathbf{F}_{ij}^n = \mathbf{F}_{ij,el} + \mathbf{F}_{ij,dn} = \frac{k_n}{N} \sum_{l=1}^{N_c} \delta_{ij,l} + \frac{2\gamma_n M}{N} \sum_{l=1}^{N} \dot{\delta}_{ij,l} \tag{20}$$

where $\delta_{ij,l}$ is the overlap at each contact point $l \in\, <0, N_c-1>$. Assuming $\delta_{ij,0} = ... = \delta_{ij,N_c-1} = \delta$, we recover EQ. (11) and hence expressions EQ. (12), EQ. (13), EQ. (15) and EQ. (16) are still valid in the case of a multi-contact point problem. In other words, the effect of compressing/elongating multiple springs and moving multiple dampers is modified in a way that it corresponds to a single contact dynamics. The primary advantage is that, contrary to Model B, T_c and γ_n do not depend on N_c in Model A, and Δt can be estimated as in a granular flow with spherical and convex particles.

Finally, in a general contact, the tangential frictional force $\mathbf{F}_{ij,t}$ is calculated in a similar fashion, i.e., summing contributions from all contact points and dividing by N_c, such that the complete force model for a contact between two non-convex particles involving N_c contact points between their elementary components has the simple following form:

$$\mathbf{F}_{ij} = \frac{1}{N_c} \sum_{l=1}^{N_c} \mathbf{F}_{ij,l,el} + \frac{1}{N_c} \sum_{l=1}^{N_c} \mathbf{F}_{ij,l,dn} + \frac{1}{N_c} \sum_{l=1}^{N_c} \mathbf{F}_{ij,l,t} \tag{21}$$

3 Validation tests

3.1 Methodology

The methodology to validate our glued convex method is two-fold. First, we run simulations with a convex shape treated as a single standard body in Grains3D and then run additional simulations of exactly the same flow configuration with the convex shape artificially decomposed into a set of smaller convex shapes. There is almost an infinity of choices. The most intuitive choices include decomposing a cylinder into a number of thinner cylinders or a cube into 8 smaller cubes. For the sake of conciseness, we select two basic particle-wall normal impact test cases: (i) with a cylinder that admits an analytical solution and (ii) with a cube. Second, we compare our numerical simulations to our own experimental data on the flow dynamics in a drum filled with 1000 non convex 2D cross-like particles rotating at $\Omega = 6\,rpm$.

3.2 Normal cylinder-wall impact

This test case is inspired by the works of Kodam *et al.* [19] and Park [30]. It involves a cylinder impacting a flat wall in the normal direction to the wall and in a gravityless space (Fig. 6). The contact is also assumed frictionless. It is conceptually simple and very convenient for an accuracy assessment of the computed solution as it admits an analytical solution. Our goal is to compare the solutions computed with Grains3D for three representations of a cylinder to the analytical solution. These three representations are:

1. a true cylinder,
2. a composite cylinder obtained by artificially slicing the true cylinder in thinner cylinders of equal thickness and gluing them together without any overlap,
3. a glued-sphere representation of the cylinder.

The initial conditions of the test case are characterized by:
– the initial angular position θ of the cylinder with respect to the horizontal plane,
– the initial translational velocity $U = (0, 0, V_{z,g}^-)$,
– and the initial angular velocity $\omega = (0, 0, 0)$.

In other words, the pre-impact translational and angular velocity magnitude is set to $V_{z,g}^-$ and 0, respectively. From [30], the post-impact angular velocity can be written as follows:

$$\omega_y^+ = \frac{MV_{z,g}^-(1+\varepsilon)r\cos(\alpha+\theta)}{I_{yy} + Mr^2\cos^2(\alpha+\theta)} \tag{22}$$

where M is the mass of the particle, $\varepsilon = -\dfrac{V_{z,g}^-}{V_{z,g}^+}$ is the signed coefficient of restitution ($|\varepsilon| = e_n$), $V_{z,g}^-$ denotes the pre-impact velocity, α denotes the angle between the face of the cylinder and the line joining the contact point and the centre of mass, θ is the pre-impact angular position of the cylinder, I_{yy} is the moment of inertia about the y axis and $r = \sqrt{R^2 + \frac{1}{4}L^2}$ is a parameter which denotes the distance between the impact point and the centre of mass, R is the radius of the cylinder and L is the length of the cylinder (see Fig. 6). Similarly, the post-impact translational velocity reads as follows ([19,30]):

$$V_{z,g}^+ = \omega_y^+ r\cos(\alpha+\theta) - \varepsilon V_{z,g}^- \tag{23}$$

Values of physical parameters are listed in Tab. 1. As in [19], we set $V_{z,g}^- = 1\,m/s$ and vary θ, the pre-impact angular position of the cylinder.

We plot in Fig. 7 the computed post-impact translational and angular velocities as a function of the pre-impact angular position θ, for the true cylinder and the glued cylinder (regardless of model A or model B). The agreement between these two simulations is extremely satisfactory. It reveals that the glued convex method is well implemented in our code. We also compare these two quasi-similar computed solutions to the analytical solution Eq. (22)-Eq. (23). The agreement of the two computed solutions with the analytical solution is also deemed to be very good, with the largest discrepancy observed on the post-impact angular velocity at low pre-impact angular positions (Fig. 7(b)).

We now investigate more deeply the differences between the two formulations to compute the total force acting on a composite particle, the so-called model A and model B. We select a particular pre-impact angular position $\theta = 90°$ and plot in Fig. 8 the time evolution of the normal contact force exerted on the cylinder over duration contact. As expected from the formulation of model A in which the total force is the sum of the forces exerted at each contact point, model A predicts an increasing total normal force as the number of elementary cylinders N increases (note that N is also the number of contact points for $\theta = 90°$) although the magnitude of the force per elementary cylinder, i.e., per contact point, decreases. Overall, the adjustment of γ_n through Eq. (18) to get the expected restitution Coefficient e_n guarantees that the solution is correct, as shown in Fig. 7, but the main drawback of model A as predicted by Eq. (19) and supported by results of Fig. 8(a) is the decrease of the contact duration T_c with N. Consequently, the time step magnitude would have to be adjusted to the number of contact points in order to properly integrate a contact. This is a very undesirable property. Conversely, model B, that assumes that the total force exerted on the particle is the mean force over all contact points, provides a normal force magnitude, a contact duration as well as a maximum penetration depth independent of N, as shown in Fig. 8(b).

Finally, we examine in the case $\theta = 90°$ the effect of N on the accuracy of the computed solution. For both model A and model B and $N \leq 30$, FIG. 9(a) reveals that the error on the computed post-impact translational velocity is less than 0.5 %. Model B performs remarkably better than model A with an error quasi independent of N and of the order of 0.05 %. The error on the computed post-impact angular velocity plotted as a function of N in FIG. 9(b) is even more interesting. The analytical solution EQ. (22) predicts that the post-impact angular velocity is $\omega_y^+ = 0$. The true cylinder simulation predicts an articificial non-zero post-impact angular velocity. This is due to the assumption, violated here, that the contact is always a point while geometrically in this case it is a line. However, the GJK algorithm supplies a point, that randomly lies somewhere along that contact line and whose position is primarily determined by rounding numerical errors. This somehow flawed contact point creates an erroneous torque that makes the particle spin after contact. Interestingly, the composite cylinder simulation predicts a post-impact angular velocity ω_y^+ that tends to 0, the correct value, as N increases. This is simply a beneficial side effect of the distribution of the N contact points along the contact line. Torques from each contact point almost cancel out with each other and the total torque exerted on the particle tends to 0 as N increases. Admittedly, the cancelling out of torques from each contact point is enhanced by using non-overlapping elementary cylinders of same thickness as it guarantees an homogeneous distribution of the N contact points along the contact line. Slicing the cylinder in potentially overlapping elementary cylinders of variable thickness undoubtedly affects the distribution of the N contact points along the contact line. It would however lead to a presumably higher erroneous total torque only if elementary cylinders are glued together in a way that purposely breaks the natural symmetry of the cylinder with respect to its half-length plane, but there is little rationale in doing so. Once again, model B performs better than model A, although it is not entirely clear why. It might simply be due to rounding errors divided by N in model B.

Overall, the glued convex approach has been very satisfactorily validated in this cylinder-wall impact test case. Model B seems to perform better and is also conceptually more sensible as contact feature estimates (and in particular the duration of contact) from a single contact point configuration are still valid. To complete the validation of the model and as a side question, we run simulations with a glued sphere representation of the cylinder and evaluate how well the glued sphere approach performs in a simple impact test case.

We consider two composite particles made of 9 and 54 spheres, respectively, as also considered by [19] and illutrated in FIG. 10. Values of physical parameters are listed in TAB. 2. For the mass properties, one can select those of a true cylinder or those of the glued-sphere representation. [19] employed a mix of true cylinder (mass) and glued sphere (moment of inertia tensor) properties, although it is rather unclear what is the motivation for such a choice.

FIG. 11(a), FIG. 11(b), FIG. 11(c) and FIG. 11(d) show the computed solutions with 9 and 54 glued spheres. Regardless of the set of mass property parameters (true cylinder, glued spheres or a mix as in [19]), the computed solution is qualitatively the same and does not match at all the analytical solution. For 54 glued spheres, the computed solution starts to pick up the right qualitative form but is still quantitatively markedly off. As the number of glued spheres used to represent the cylinder increases, it is however predictable that the computed solution will tend to the analytical solution. It is interesting to observe that for two particular pre-impact angular position values 0° and 90°, the glued sphere representation captures the right post-impact velocities. These two angles correspond to two particular contact configurations in which the shape of the cylinder and specifically the artificial roundedness of the edges created by gluing spheres does not play any role. It fact, at 0° and 90°, the actual contact zone geometry is a surface and a line respectively. The homogeneous distribution of the glued spheres over the cylinder volume assures the proper computation of the normal contact force and the associated torque (that is 0). For all other pre-impact angular positions that lead to a single contact point, the error on the post-impact velocities is very significant, unless the number of glued spheres is large (probably of the order of $O(10^2 - 10^3)$, as a result of the artificial rounded edges of the glued-sphere representation of the cylinder. In general, this simple test case reveals that the glued sphere representation of a complex shape, also intuitively attractive, might provide computed solutions of very weak accuracy and should hence be used with great care, if not prohibited.

3.3 Normal cube-wall impact

Our second particle-wall impact validation test pertains to a cube of edge length $2\times10^{-3}m = 2mm$ impacting a flat wall under gravity. The particle is released from an initial height of $0.08m$, i.e., 40 times the cube edge length, with various initial angular positions. The cubic particle accelerates while free falling under gravity until it impacts and bounces on the flat wall. We set the coefficient of restitution to $e_n = 0.9$ such that energy is dissipated over each collision. Thus the particle progressively reaches a lower height following multiple collisions with the bottom wall until it rests motionless on the bottom wall. We also consider the collision to be frictionless. Contrary to the cylinder-wall investigated in *Section 3.2*, the problem of the normal cube-wall impact under gravity does not possess any analytical solution, hence we consider the predictions with a standard cubic particle as a reference. We perform two sets of simulation with the following corresponding representation of the cube:

1. a true cube,
2. a glued convex cube obtained by artificially slicing the cube into 8 smaller cubes of equal size and gluing them together without any overlap.

Gravity is prescribed downwards along the z (vertical) direction and we consider the following initial angular positions $(\theta_x, \theta_y) = (0^o, 0^o), (10^o, 10^o), (25^o, 25^o), (75^o, 75^o)$ and $(30^o, 0^o)$, where θ_x and θ_y denote the initial angular position of the cube with respect to the x axis and the y axis, respectively. Numerical parameters are listed in TAB. 3. We use Model B for the glued convex cube and the exact mass properties for both representations of the cube.

We plot in FIG. 12 the time evolution over the 2 first impacts of the particle vertical position and the x-component of the particle angular velocity for both the true cube and the glued convex cube. When the impact does not correspond to a perfect face-wall geometric configuration $(\theta_x, \theta_y) = (0^o, 0^o)$ or a perfect edge-wall geometric configuration $(\theta_x, \theta_y) = (30^o, 0^o)$, FIG. 12 shows that numerical predictions for the glued convex cube are in quasi-perfect agreement with numerical predictions for the true cube. As for the normal cylinder-wall impact with $\theta = 90^o$ examined in *Section 3.2*, the perfect edge-wall geometric configuration involves a contact line and the single contact point assumption used by the true cube model is not satisfactory as it creates an erroneous torque leading to artificial particle rotation after contact. The glued convex cube generally performs better as, being made of 8 twice smaller cubes, the contact line is now modelled with 2 contact points that cancel out the erroneous artificial torque. The same comment applies to a perfect face-wall geometric configuration $(\theta_x, \theta_y) = (0^o, 0^o)$ where the contact surface is modelled with 4 contact points for the glued convex cube compared to a single contact point that randomly lies somewhere along that contact surface and whose position is primarily determined by rounding numerical errors. As for the cylinder in *Section 3.2*, what matters is to preserve the natural summetry of the cube when decomposing it into a set of potentially overlapping smaller cubes. In fact, in FIG. 12(b), ω_x is still uniformely 0 after 2 collisions for the glued convex cube while it has artificially (and primarily physically wrong) non-zero values for the true cube. This is a general weakness of the single contact point assumption that the glued convex approach coincidentally contributes to solve. However, it is computationally not desirable to slice a simple convex shape into a set of smaller elementary convex shapes as the computational overhead is rather prohibitive.

Based on the comments above about the modelling of contact lines or surfaces, it is more rationale from a physical viewpoint to assume that the reference solution is the solution obtained with the glued convex cube. Interestingly the first impact is always well predicted even by the true cube with a single contact point, but then the small amplitude erroneous rotation propagates and the next impact is more significantly affected. As a final comment, we would like to point out that after multiple impacts, the true cube and the glued convex cube solutions eventually always differ due to the propagation of rounding errors by the explicit time integration algorithm and approximations in geometric operations performed by the GJK algorithm. These small amplitude numerical uncertainties have however no visible impact on the dynamics of a system containing many particles.

3.4 Validation against experimental data: 1000 2D cross-like particles in a drum rotating at $\Omega = 6\,rpm$

Here we compare simulation results to experimental data in a rotating drum configuration. Our non-convex particles are tile spacers (Fig. 13) that can be found in the construction industry. Tile spacers have a 2D-cross like shape and exhibit a high concavity and angularity. They hence represent a good candidate for a challenging test case for our code Grains3D. In addition, they are cheap (they can be bought for around 10$ a box of a thousand by any local renovation warehouse) such that any other research group can easily reproduce this experiment. Please note that our tile spacers are made of plastic and are slightly deformable. However, with the level of stress load applied to particles in such a small system, particle deformations are so small that particles can safely be considered as fully rigid (in a larger system this assumption might be violated as the granular pressure at the bottom might be large enough to locally deform particles).

The experimental set-up is a rotating drum with transparent plexiglas walls. The back circular wall is made of rough plastic and can be adjusted to have the desired drum width. In our study, the drum has a diameter $D = 30\,cm$ and a width $W = 7\,cm$. It is filled with 1000 plastic tile spacers (see Fig. 14). Simulation parameters are listed in Tab. 4. Please note that contact parameters (e_n, μ_c) have not been tuned to improve the agreement between experimental data and simulation results. We simply select parameters roughly representative of plastic-plexiglas contacts. We anyway believe that in such a system the dynamics is primarily governed by the intricate microstructure of the particles pack and not by the magnitude of the contact parameters (in other words changing μ_c from, e.g., 0.4 to 0.6 will only mildly change the overall system behavior). We set the rotation rate to $\Omega = 6\,rpm$.

The resulting dynamics is largely dominated by episodic avalanching at this rotation rate (see *Section 4.2* for more detail about flow regimes) and the free surface is hard to define. In any case, it does not look like a flat surface and makes the definition of the dynamic angle of repose quite complicated. Another marker of the flow that would be of high interest is the episodic avalanching frequency but once again it is not easy to determine. At that stage, we only show a comparison of the time evolution of the free surface obtained by image processing. Our image processing works as follows. We first convert all images resulting from numerical simulation and experiments into binary images of white and black pixels. To this end, we change the coloured images into grey scale images, then we apply a threshold equal to 255 to convert them into binary images. The free surface can be determined in two ways: (i) by plotting the real free surface or (ii) by plotting a polynomial fitting function of high order. For the sake of simplicity, we choose the former option. The experimental camera captures 40 frames per second and our simulation is set to create outputs at the corresponding time frequency, i.e. every $\Delta t = 0.025\,s$. Please note that due to the shadow created by the light shed from the front in the experimental set-up, the threshold of 255 on all images can hide some particles in the back of the drum, yielding a visually less dense bed compared to the bed in simulation results. This is a biased impression and the pack of particles has indeed the same density in numerical simulation and experiments.

Both the movie (uploaded as supplementary material) and Fig. 16 show a strikingly satisfactory agreement of numerical results with experimental data. This indicates that Grains3D is capable of faithfully reproducing the overall complex dynamics of a system of particles with a rather complicated non-convex shape. An on-going work in our group is to define and compute other quantitative markers of the flow as, e.g., the frequency spectrum of the avalanching process or the time evolution of the gravity center of the pack of particles, to validate even further this test case. But this preliminary comparison is already very promising.

4 Results

4.1 Packing porosity

Void fraction or porosity of a (static) packing of granular material is simply the measure of the ratio of the volume of empty space to the total volume of the system. Compacity corresponds to the opposite of porosity and represents the ratio of total volume of particles to total volume of the system. Compacity of convex particles packings can be estimated by computing the Voronoï diagram of the system [26] whereas for non-convex particles the use of this method is impeded by

their concavity. Consequently, another method has to be used for the characterization of compacity of random packings of non-convex particles. Here we use the same method as the one used to calculate the mass properties of a non-convex particle, i.e., we define a box embedding the packing of particles, pixelate that space with a fine cartesian constant grid size structured mesh and approximate the volume integral of the space actually occupied by particles by summing all the cells of the fine cartesian mesh whose center lies inside a particle. The method is fully parallelised as the total number of cells in this fine cartesian mesh is very often of the order of $O(10^8 - 10^9)$ to guarantee a sufficient level of accuracy.

Packings are created by inserting particles at the top of the domain. Particles settle downwards by gravity and collide with neighbouring particles and/or the bottom wall. The filling process is deemed to be complete when all particles reach a pseudo stationary state characterized by a negligible total kinetic energy of the system. We consider the two following configurations:

1. a system without lateral solid wall effects designed as a box with bi-periodic boundary conditions on the lateral (vertical) boundaries, i.e., in the horizontal directions. 1000 particles are inserted in the simulation in the following way: (i) a particle position is randomly selected in a thin parallelepiped at the top of the domain at each time t^n, (ii) a random angular position is assigned to the particle, (iii) insertion is attempted. If successful, the particle is inserted, otherwise a new random position together with a new random angular position is selected and insertion is attempted again at the next time t^{n+1}. This insertion procedure results in a moderately dense shower of particles stemming from the parallelepipedic insertion window.
2. a system with strong lateral wall effecs designed as a cylindrical reactor with a circular cross-section. We select the same configuration as in our previous work [39]. In [39], we examined the effect of convexity on packing porosity. Now we extend this case study to non-convexity. 250 particles are randomly inserted at the top of the domain at a flow rate of 1 particle per second until the simulation is stopped at 260 s. Lateral wall effects are deemed to be strong as the reactor diameter to particle equivalent diameter ratio is $\approx 50/8 = 6.25$, an admittedly small value.

In both configurations, we consider the 4 convex shapes already examined in [39] in addition to two new non-convex cross-like shapes illustrated in FIG. 17. All shapes have the same volume. The two meaningful physical parameters of the contact force model are set to $e_n = 0.73$ and $\mu_c = 0.55$.

Packings of the different shapes in the wall-free bi-periodic domain are presented in FIG. 18. The corresponding porosities computed by our approximate numerical integration based on pixelating the space occupied by the packing of particles are shown in TAB. 5. Although tetrahedra already exhibit a slightly higher porosity, there is a remarkable jump of porosity between the 4 convex shapes and the 2 non-convex cross-like shapes. In fact, ε for 3D crosses is twice larger than that for spheres of same volume.

With strong wall effects, the effect of shape on porosity ε is even more emphasised, as illustrated by FIG. 19. Porosity varies linearly with the height of the bed, and visually the variation of bed height as a function of shape speaks for itself. Bed height for 3D crosses (blue particles in FIG. 19(f)) is literally 5 times larger than that for spheres, cylinders and cubes, translating into a 5 times larger porosity. It is also 4 times larger than that for tetrahedra as well as 2 times larger than that for 2D crosses. For 3D crosses, it is quite remarkable in FIG. 19(f) that ε is close to 1 close to the reactor wall in a crown of width approximately half the length of the cross beams, whereas all other shapes, even 2D crosses, are able to fill that region much better. Obviously, we have selected these 2 non-convex shapes on purpose, as they exhibit a low sphericity and promote some sort of entanglement in the packing. They are hence good candidates for high porosity packings and other unusual intricate effects in granular dynamics as we shall see in the next section. The analysis of the packing micro-structure can be easily extended e.g. by looking at the porosity radial profile, by this goes beyond the scope of the present paper. Our goal here is primarily to evaluate quantitatively packing porosity for such shapes and to shed some light on how strong the effect of shape can be, even in a very simple configuration.

4.2 Rotating drum

Following [44,43,39] we investigate the flow dynamics of a granular media in a rotating drum. We select the same flow configuration as in our previous work [39] and our goal is to extend results

previously obtained for convex particles to non-convex particles. As in [39], the drum has a radius of $R_{drum} = 50\,mm$ and a depth of $24\,mm$. A periodic boundary condition is applied along the drum axis to avoid end wall effects. The drum is loaded with mono-dispersed non-convex particles such that the region occupied by particles in the drum (regardless of porosity) corresponds to 35% of the drum volume, i.e. the pack has initially a height equal to $\approx 0.76R_{drum}$. For the non-convex shapes, we use the same 2D and 3D crosses as in *Section 4.1*. The new simulation results for the 2D and 3D crosses complement the existing set of results we obtained for convex particles (i.e., spheres, cylinders, cubes and regular tetrahedron) in [39]. Once again, all shapes have the same volume, that corresponds here to a sphere with a radius of $R_e = 1.5\,mm$. Values of all simulation parameters are listed in TAB. 6.

As shown in *Section 4.1* for the non-convex cross-like shapes and in [39] for tetrahedra, the total number of particles for each shape need to be adjusted such that the initial bed height is always $\approx 0.76R_{drum}$ (35% of the drum volume) due to the high variations in porosity between shapes. While the drum was loaded with 3000 spheres, cylinders and cubes, only 2600 regular tetrahedra were used in [39]. Here, we fill the drum with 1500 2D crosses and 1250 3D crosses.

4.2.1 3D cross shape

FIG. 20 shows the internal flow structure of a system filled with 3D crosses for $\Omega \in [5; 250]\,rpm$. A first sight already indicates the strong influence of the particle shape on the flow dynamics, compared to spheres and even to convex particles. Similarly to the filling process in *Section 4.1*, the significant differences observed all result from the ability of 3D crosses to entangle. As for other convex shapes, we observe a transition from an avalanching regime to a cataracting regime, then to a pseudo-cataracting and eventually to a centrifuging regimes as the rotation rate increases. Note that for low rotation rates, the rolling regime observed for spheres is replaced by an avalanching regime (the same was observed for convex shapes in [39]). Let us now describe qualitatively the features of each flow regime.

At $\Omega = 5\,rpm$, the flow regime is representative of episodic avalanches governed by the pseudo-chaotic evolution of the highly entangled micro-structure of the pack of particles. Particle rotation is strongly impeded both close to the drum wall and at the free surface. As for other shapes, particles close to the drum wall experience a rigid body motion while the major difference occurs at the free surface. Particles entanglements delay the onset of avalanching up to very high free surface angles, sometimes close to 90°. Then the pack eventually breaks and big clusters of particles detach and fall down from the top right to the bottom left of the free surface. Big cluster detachment from the rest of the pack of particles at the top right resembles to some extent the fracturing of an inhomogeneous solid material or a cohesive granular media. Fracturing starts at the location in the pack that shows a weakness characterized by a lower level of entanglement, i.e., a lower level of cohesion. We call this regime episodic avalanching as the frequency of occurrence of avalanches is less regular and hence tougher to define than for convex shapes, as supported by FIG. 26. As the rotation rate increases to $\Omega = 20\,rpm$, big clusters of particles at the free surface disappear to give way to a thick layer of particles flowing down the free surface from the top right to the bottom left. At $\Omega = 80\,rpm$, particles gain enough kinetic energy to start freeing themselves from the pack. Flow dynamics is still strongly governed by particles entanglements but the pack of particles is not as dense anymore and consequently the strength or cohesion of the pack of entangled particles is weaker. This corresponds to a transition from avalanching to cataracting, although particles at the free surface do not yet have a free-fly ballistic motion. At $\Omega = 125\,rpm$, the kinetic energy of particles at the top right of the free surface is large enough for them to almost free themselves from the pack and free fly. This flow dynamics is a typical sign of a cataracting regime [27]. We would like to make a short digression of the determination of the onset of cataracting regime. As a comparison, we observe this ballistic trajectory of spherical particles in the range $150\,rpm \le \Omega \le 200\,rpm$, which suggests that cataracting regime starts at about $150\,rpm$ for spheres. From FIG. 20, we might define the onset of cataracting regime at $\Omega = 125\,rpm$, which would hence indicate that 3D crosses exhibit a cataracting regime at lower rotation rates than spheres. At $\Omega = 125\,rpm$ the Froude number defined as $\Omega^2 R_{drum}/g$ is $\mathcal{F}r \simeq 0.87$. Looking more closely at FIG. 20(d), the notion of free-flight is tougher to define. Although the overall flow pattern does look like a cataracting regime, particle that detach from the top right still seem to be linked together with neighbouring particles in their pseudo free-flight in a very weak way. For spheres (see [39]-Fig5(e)), it is very visible that particles flying from the top right to the bottom left of the free surface do not touch any other neighbouring

15

particles. In other words, the transition from avalanching to cataracting is not necessarily easy to determine for 3D crosses. From $\Omega = 150\,rpm$, the cataracting regime starts to disappear and is progressively replaced by a pseudo-cataracting (or pseudo-centrifuging) regime. Ω is not high enough to already observe a fully centrifuging regime but not low enough for the cataracting regime to persist. The thin layer empty of particles at the top of the drum is a signature that the full centrifuging regime has not yet been attained. At $\Omega = 150\,rpm$, the Froude number is $\mathcal{F}r \simeq 1.25$. Finally, from $\Omega = 200\,rpm$, the fully centrifuging regime manifests, corresponding to $\mathcal{F}r \simeq 2.25$. For spheres, we determined in [39] that the transition to centrifuging regime occurs at $\Omega \simeq 220\,rpm$, i.e., for $\mathcal{F}r \simeq 2.7$. This would suggest that the transition from cataracting to centrifuging occurs at lower rotation rates for 3D crosses than for spheres. As already noticed for spheres or any other shapes, the centrifuging regime is characterized by a continuous layer of particles attached to the drum wall and rotating with the drum as a rigid body. A particular and rather fascinating feature of 3D crosses is the form of the free surface of the pack of particles undergoing a rigid body motion. While for spheres this layer has a constant thickness, it is rather irregular for 3D crosses. Actually, the entangled 3D crosses create an imprint over the early transients of the drum rotation. In other words, the free surface is determined by a competition between the strength or cohesion of the entangled pack of particles and the centrifugal force that pushes particles towards the drum wall. The free surface very rapidly adopts its final form (after a few drum rotations only) and then remains forever frozen in a rigid body rotation as shown in FIG. 20(f).

To illustate how much the 3D cross-like shape hinders the rotation of a particle compared to a sphere, even without entanglements with neighbouring particles, we perform a simulation of a single particle in the drum rotating at $\Omega = 150\,rpm$ (FIG. 21). The resistance to rolling motion of the sphere is very low and accordingly the critical angle at which the sphere starts to roll down the drum wall is very low too. 3D cross reaches much higher on the top right and their overall motion is far more chaotic. The ratio of translational to angular kinetic energy is much higher for a 3D cross than for a sphere. It would be interesting to extract this ratio in the multi-particle rotating drum simulations to shed some more light on differences in energy conversion mechanism between sphere, convex and non-convex shapes. This is an on-going work in our group and will be the topic on a future paper.

We illustrate in FIG. 22 the avalanching nature of the flow dynamics at low rotation rates $\Omega = 5\,rpm$ and $\Omega = 20\,rpm$. In particular at $\Omega = 5\,rpm$, we can neatly see in FIG. 20(a)(c) that the shallow layer of slumping particles at the free surface fractures in the middle into two big clusters. Another important comment concerns the determination of the dynamic angle of repose of the free surface in this avalanching regime. In fact, not only the free surface is anything but a flat surface but the flow is highly intermittent (episodic) and the dynamic angle of repose varies over time with a large amplitude. In FIG. 20(a)(c), it is noticeable that the free surface is close to vertical.

4.2.2 2D cross shape

The overall picture of 2D crosses is qualitatively similar to the picture of 3D crosses. Since 2D crosses have a higher sphericity than 3D crosses and a lower tendency to entangle, the original features observed for 3D crosses are also observed but less marked for 2D crosses. We notice the same transitions from avalanching to cataracting, then to pseudo-cataracting and eventually to centrifuging as the drum rotation rate increases, but these transitions occur for slightly different critical rotation rates. The different flow regimes for 2D crosses are shown in FIG. 23.

In general, the pack of 2D crosses is less cohesive than the pack of 3D crosses, in the sense that the strength of the entangled network of particles is weaker. This difference manifests very visibly in FIG. 24 where we illustrate the transient flow dynamics in the drum. The dynamic angle of repose of 2D crosses, although pretty high compared to convex shapes, is lower than that of 3D crosses. It also seems that the free surface, although not very flat, is significantly flatter than that of 3D crosses. Finally, FIG. 26 suggests that avalanches are more regular and that the avalanching regime can be classified as periodic avalanching, in contrast to episodic avalanching for 3D crosses. At $\Omega = 5\,rpm$ a single avalanching frequency for 2D crosses can be more clearly defined than for 3D crosses, although this is not totally obvious. Finally, cataracting, pseudo-cataracting and centrifuging regimes of 2D crosses are very similar to those of 3D crosses.

4.2.3 Further comments

We plot in FIG. 25 the averaged in time coordination number as a function of rotation rate for all shapes. In general, 2D and 3D crosses exhibit a higher coordination number than other shapes regardless of the rotation rate, as a result of the highly entangled micro-structure. However, up to $\Omega = 150\,rpm$, the trend is very similar to convex particles and there is no major signature of non-convexity in the variation of the coordination number with Ω. The plots for the 2 non-convex shapes are simply shifted to higher values of coordination number. The only signature of non-convexity pertains to the transition to cataracting/pseudo-cataracting regime and then to centrifuging regime. However, we run additional simulations for tetrahedra and notice the same trend than that for 2D/3D crosses. Hence, this suggests that this signature is actually not relevant of non-convexity only, but more generally of non-sphericity. This emphasizes again that the transitions to cataracting/pseudo-cataracting and to centrifuging are not easy to define. The increase of the coordination number above $\Omega = 150\,rpm$ might however indicate the onset of transition to centrifuging. At high $\Omega \geq 200\,rpm$, the absence of a neat plateau (as visible as for spheres) does not allow us to determine from this plot only when the fully centrifuging regime really starts.

We plot in FIG. 26 the mean dimensionless translational particle velocity as a function of time for different rotation rates. The interesting and already described in the above features of 2D and 3D crosses flow dynamics occur at low rotation rates $\Omega = 5rpm$ and $\Omega = 20rpm$. From $\Omega = 42rpm$, the mean translational particle velocity of the 2 non-convex shapes is very similar to that of any of the 3 non-spherical convex shapes. $\Omega = 5\,rpm$ reveals that 3D crosses undergo more chaotic, in the sense of larger amplitude and more episodic, avalanches than 2D crosses and convex shapes. The peaks of mean translational particle velocity represent rapid avalanches of particles triggered by a very high dynamic angle of repose (up to $\sim 90°$). The most remarkable manifestation of resistance to slump or to flow from the top right to the bottom left of the drum of the highly entangled pack of 3D crosses occurs at $\Omega = 20\,rpm$. While 2D crosses and cubes both exhibit a moderate avalanching dynamics, 3D crosses still undergo large amplitude and well defined avalanches characterized by large amplitude fluctuations of the mean translational particle velocity with time. At high rotation rates, the mean translational particle velocity progressively tends to a constant value over time. For instance, at $\Omega = 200\,rpm$, the mean translational particle velocity does not vary with time anymore. This represents a much more reliable signature of the onset of fully centrifuging regime than what we could extract from the coordination number analysis.

Finally, we compute the Probability Density Function (PDF) of the time averaged dimensionless translational particle velocity in an attempt to capture some additional signatures of regime transition, and in particular of the transitions to pseudo-cataracting/cataracting and to centrifuging. This analysis created incentives to run additional simulations in the range $\Omega \in [100; 200]\,rpm$. We select $\Omega = 100\,rpm$, $\Omega = 120\,rpm$, $\Omega = 165\,rpm$ and $\Omega = 180\,rpm$ for the 2D/3D crosses to complement our set of results. For $\Omega < 100\,rpm$, the PDFs for both shapes presented in FIGS. 27(a) and 27(c) look very similar and it is not easy to observe any visible trend that would delineate avalanching from cascading and cascading from cataracting. In fact most particles move with a translational velocity lower than $\Omega \mathbf{R}_{drum}$ and the long tail of low PDF values for $\Omega > \mathbf{R}_{drum}$ correspond to the avalanching/cascading particles close to the free surface. Note however that as $\Omega \in [5; 100]\,rpm$ increases PDF values in this tail increase too, indicating a progressive shift from avalanching to cascading. The transitions to pseudo-cataracting and centrifuging are conversely very visible in FIGS. 27(b) and 27(d) as the PDFs significantly narrow. The fact that 2D cross PDFs are generally narrower for $\Omega > 150\,rpm$ is due to the free surface of the pack of particles and the particles volume fraction in the pack. Once again, this free surface is controlled by the early transients and the higher level of cohesion of 3D crosses leads to a more irregular free-surface than that for 2D crosses. Interestingly, in the range $\Omega \in [150; 165]\,rpm$, for both shapes, the pseudo-stationary regime is quasi-centrifuging, with only a few (less than 5 in any cases) particles plummeting from the highest point of the free surface to the bottom of the free surface, but the transient regime is much longer than for any other cases investigated. For instance, for 2D crosses and $\Omega = 165\,rpm$, about 20 drum rotations are necessary to establish the quasi-centrifuging regime, as shown in FIG. 28.

5 Conclusion and discussion

We suggested an extension of our DEM from convex to non-convex shapes. As a reference to the glued spheres model, the novel method is called *glued convex* method as convex particles are "glued" together to create any non-convex shape. Our novel method for non-convex shapes relies on the same tools we used for convex shapes in [39]. In fact, contact detection between two non-convex bodies relies on contact detection between all the pairs of elementary convex components that compose each composite non-convex body. This reduces the complexity of the problem of contact detection between non-convex bodies to the problem of contact detection between convex bodies, a problem for which we have already suggested a reliable and accurate solution method in Grains3D-Part I [39] using a Gilbert-Johnson-Keerthi algorithm. The novel method is extremely versatile as virtually any non-convex shape can be considered. We illustrated the new simulation capabilities of our in-house code Grains3D in two flow configurations: (i) filling of a reactor and (ii) flow dynamics in a rotating drum. The simulation results we presented for non-convex 2D and 3D crosses are unprecedented in the literature.

We suggested a simple but robust solution to the problem of multi-contact points that enables us to keep using analytical estimates of contact features and in particular of contact duration. This significantly facilitates the estimation of the time-step magnitude in DEM simulations of non-convex bodies. We considered a normal cylinder-wall impact test case to illustrate the validation of our implementation. Along the way, we confirmed, as other works of the literature already showed [19], that the accuracy of the glued sphere method to model particles of arbitrary shape is highly questionable as it rounds sharp angles and introduce an artificial rugosity. Conversely, our glued convex approach preserves angularity since a non-convex composite particle is decomposed into a set of elementary convex shapes, that are by essence sharp. A side effect of composite particles is their intrinsic ability to better handle contact configurations in which the contact zone cannot be modelled as a point, but rather as a line or a surface. In fact, composite particles naturally introduce multiple contact points corresponding to the contact points of their elementary components. Although decomposing an already convex particle in a set of smaller elementary convex particles is not the most promising path from a computational viewpoint, this property can still be exploited to improve the stability of, e.g., static heaps of particles and somehow circumvent the conceptual inability of our Gilbert-Johnson-Keerthi -based contact detection strategy to provide a line of contact, a surface of contact or multiple contact points from two simple convex bodies that overlap.

Although our DEM for non-convex bodies opens up unprecedented numerical modelling perspectives, the computing cost is still prohibitive. In fact, the computing cost of contact detection between two non-convex bodies scales as $N \times M$, where N denotes the number of elementary components of the first particle and M that of the second particle. Another computational drawback of the current implementation is that potential contacts are assessed with the circumscribed sphere to the non-convex particles, and then if they overlap with the circumscribed sphere to the convex elementary components (see FIG. 29). If the non-convex or elementary convex bodies are elongated, our method is not optimised and many contacts that actually do not exist are considered at the detection step. This undesirably slows down computations. An alternative solution would be to use oriented bounding boxes, with however no guarantee that the overall computing time will be lower as an oriented bounding box overlap test is more time consuming than a two sphere overlap test. We believe that contact detection between two non-convex bodies should be speeded up at the serial level.

Potential applications of Grains3D were already quite broad, and our *glued convex* model broadens even more its range of applicability. Only two examples of application were considered in this study that adequately illustrated the visible effect of particle non-convex shape on flow dynamics. Results from the rotating drum as shown in FIGS. 25 and 26 emphasize how flow dynamics differs from convex particles to non-convex particles. In order to summarize our study, we plot a tentative map of rotating drum flow regimes in FIG. 30. Values of critical Ω for regime transitions are qualitative only, as hard to determine unambiguously. Also please note that this qualitative flow map is drawn for a given filling ratio ($\simeq 0.35$) and a given drum size to particle size ratio ($\simeq 17$). Changing these two values would certainly change the flow map. The rolling regime disappears progressively as the angularity of the particle increases. It is replaced by an avalanching regime whose range of occurence increases with angularity. We found a somehow similar rotation rate range for cascading regime for all angular particles investigated, regardless of convexity/non-

convexity. A pseudo-cataracting regime appears between the cataracting and centrifuging regimes for highly concave bodies. The centrifuging regime appears earlier for angular particles compared to spherical particles. Indeed, our results, although unprecedented, are a first step only towards an enhanced comprehension of the effect of angularity on the flow dynamics in a rotating drum. Our analysis can easily be extended to gain more insight into regime transitions and overall flow dynamics.

Acknowledgement

On behalf of all authors, the corresponding author states that there is no conflict of interest.

References

1. M. Abbaspour-Fard. Theoretical validation of a multi-sphere, discrete element model suitable for biomaterials handling simulation. *Biosystems Engineering*, 88(2):153 – 161, 2004.
2. F. Alonso-Marroquín and Y. Wang. An efficient algorithm for granular dynamics simulations with complex-shaped objects. *Granular Matter*, 11(5):317–329, 2009.
3. H. Bekker and J. B. Roerdink. An efficient algorithm to calculate the minkowski sum of convex 3d polyhedra. In *Computational Science–ICCS 2001*, pages 619–628. Springer, 2001.
4. F. Camborde, C. Mariotti, and F. Donzé. Numerical study of rock and concrete behaviour by discrete element modelling. *Computers and geotechnics*, 27(4):225–247, 2000.
5. E. Coumans. *Bullet 2.83 Physics Library manual*, 2015.
6. P. Cundall and O. Strack. A discrete numerical model for granular assemblies. *Geotechnique*, 29(1):47–65, 1979.
7. P. A. Cundall. Formulation of a three-dimensional distinct element model–Part I. A scheme to detect and represent contacts in a system composed of many polyhedral blocks. *International Journal of Rock Mechanics and Mining Sciences & Geomechanics Abstracts*, 25(3):107–116, 1988.
8. R. Doe. *CGAL, Computational Geometry Algorithms Library*, jun 2009.
9. A. Džiugys and B. Peters. An approach to simulate the motion of spherical and non-spherical fuel particles in combustion chambers. *Granular matter*, 3(4):231–266, 2001.
10. Y. Feng and D. Owen. A 2D polygon/polygon contact model: algorithmic aspects. *Engineering Computations*, 21(2/3/4):265–277, 2004.
11. F. Y. Fraige, P. A. Langston, and G. Z. Chen. Distinct element modelling of cubic particle packing and flow. *Powder Technology*, 186(3):224–240, 2008.
12. E. G. Gilbert and C. Foo. Computing the distance between general convex objects in three-dimensional space. *Robotics and Automation, IEEE Transactions on*, 6(1):53–61, 1990.
13. E. G. Gilbert, D. W. Johnson, and S. S. Keerthi. A fast procedure for computing the distance between complex objects in three-dimensional space. *Robotics and Automation, IEEE Journal of*, 4(2):193–203, 1988.
14. R. Hart, P. Cundall, and J. Lemos. Formulation of a three-dimensional distinct element model–Part II. Mechanical calculations for motion and interaction of a system composed of many polyhedral blocks. In *International Journal of Rock Mechanics and Mining Sciences & Geomechanics Abstracts*, volume 25, pages 117–125. Elsevier, 1988.
15. S. Hentz, L. Daudeville, and F. V. Donzé. Identification and validation of a discrete element model for concrete. *Journal of engineering mechanics*, 130(6):709–719, 2004.
16. D. Höhner, S. Wirtz, H. Kruggel-Emden, and V. Scherer. Comparison of the multi-sphere and polyhedral approach to simulate non-spherical particles within the discrete element method: Influence on temporal force evolution for multiple contacts. *Powder Technology*, 208(3):643 – 656, 2011.
17. F. Jin, H. Xin, C. Zhang, and Q. Sun. Probability-based contact algorithm for non-spherical particles in DEM. *Powder Technology*, 212(1):134–144, 2011.
18. L. Jing. Formulation of discontinuous deformation analysis (dda)–an implicit discrete element model for block systems. *Engineering Geology*, 49(3):371–381, 1998.
19. M. Kodam, R. Bharadwaj, J. Curtis, B. Hancock, and C. Wassgren. Cylindrical object contact detection for use in discrete element method simulations. part II–Experimental validation. *Chemical Engineering Science*, 65(22):5863–5871, 2010.
20. H. Kruggel-Emden, S. Rickelt, S. Wirtz, and V. Scherer. A study on the validity of the multi-sphere discrete element method. *Powder Technology*, 188(2):153 – 165, 2008.
21. P. Langston, U. Tüzün, and D. Heyes. Continuous potential discrete particle simulations of stress and velocity fields in hoppers: transition from fluid to granular flow. *Chemical Engineering Science*, 49(8):1259–1275, 1994.
22. P. Langston, U. Tüzün, and D. Heyes. Discrete element simulation of granular flow in 2d and 3d hoppers: Dependence of discharge rate and wall stress on particle interactions. *Chemical Engineering Science*, 50(6):967–987, 1995.
23. Y. Lee, C. Fang, Y.-R. Tsou, L.-S. Lu, and C.-T. Yang. A packing algorithm for three-dimensional convex particles. *Granular Matter*, 11(5):307–315, 2009.
24. J. Li, P. A. Langston, C. Webb, and T. Dyakowski. Flow of sphero-disc particles in rectangular hoppers–a DEM and experimental comparison in 3D. *Chemical Engineering Science*, 59(24):5917–5929, 2004.
25. G. Lu, J. Third, and C. Müller. Discrete element models for non-spherical particle systems: From theoretical developments to applications. *Chemical Engineering Science*, 127:425–465, 2015.
26. V. Luchnikov, N. Medvedev, L. Oger, and J.-P. Troadec. Voronoi-delaunay analysis of voids in systems of nonspherical particles. *Phys. Rev. E*, 59:7205–7212, Jun 1999.
27. J. Mellmann. The transverse motion of solids in rotating cylinders–forms of motion and transition behavior. *Powder Technology*, 118(3):251 – 270, 2001.
28. A. Munjiza, J. F. Peters, M. A. Hopkins, R. Kala, and R. E. Wahl. A poly-ellipsoid particle for non-spherical discrete element method. *Engineering Computations*, 26(6):645–657, 2009.
29. G. Nolan and P. Kavanagh. Random packing of nonspherical particles. *Powder technology*, 84(3):199–205, 1995.
30. J. Park. *Modeling the dynamics of fabric in a rotationg horizontal drum*. PhD thesis, Purdue University, 2003.
31. D. Petit, F. Pradel, G. Ferrer, and Y. Meimon. Shape effect of grain in a granular flow. *Powders and grains*, page 425, 2001.
32. L. Pournin and T. Liebling. A generalization of Distinct Element Method to tridimensional particles with complex shapes. In *Powders and Grains*, volume 5805, pages 1375–1378. R García-Rojo, H J Herrmann, and S McNamara, 2005.
33. A. D. Rakotonirina and A. Wachs. Grains3D, a flexible DEM approach for particles of arbitrary convex shape - Part II: parallel implementation and scalable performance. *Submitted to Powder Technology*, 2016.
34. S. Rémond, J. Gallias, and A. Mizrahi. Simulation of the packing of granular mixtures of non-convex particles and voids characterization. *Granular Matter*, 10(3):157–170, 2008.
35. Y. Song, R. Turton, and F. Kayihan. Contact detection algorithms for DEM simulations of tablet-shaped particles. *Powder Technology*, 161(1):32–40, 2006.

36. H. Tangri, Y. Guo, and J. Curtis. Packing of cylindrical particles: DEM simulations and experimental measurements. *Powder Technology*, 317:72–82, 2017.
37. G. van den Bergen. A fast and robust GJK implementation for collision detection of convex objects. *Journal of Graphics Tools*, 4(2):7–25, 1999.
38. A. Wachs. A DEM-DLM/FD method for direct numerical simulation of particulate flows: Sedimentation of polygonal isometric particles in a Newtonian fluid with collisions. *Computers & Fluids*, 38(8):1608–1628, 2009.
39. A. Wachs, L. Girolami, G. Vinay, and G. Ferrer. Grains3D, a flexible DEM approach for particles of arbitrary convex shape–Part I: Numerical model and validations. *Powder Technology*, 224:374–389, 2012.
40. J. R. Williams and R. O'Connor. A linear complexity intersection algorithm for discrete element simulation of arbitrary geometries. *Engineering computations*, 12(2):185–201, 1995.
41. J. R. Williams and A. P. Pentland. Superquadrics and modal dynamics for discrete elements in interactive design. *Engineering Computations*, 9(2):115–127, 1992.
42. Y. Wu, X. An, and A. Yu. DEM simulation of cubical particle packing under mechanical vibration. *Powder Technology*, 314:89–101, 2017.
43. R. Yang, A. Yu, L. McElroy, and J. Bao. Numerical simulation of particle dynamics in different flow regimes in a rotating drum. *Powder Technology*, 188(2):170–177, 2008.
44. R. Yang, R. Zou, and A. Yu. Microdynamic analysis of particle flow in a horizontal rotating drum. *Powder Technology*, 130(1-3):138–146, 2003.
45. B. Zhao, X. An, Y. Wang, Q. Qian, X. Yang, and X. Sun. DEM dynamic simulation of tetrahedral particle packing under 3D mechanical vibration. *Powder Technology*, 317:171–180, 2017.

List of Tables

Parameter	True cylinder	Glued cylinders	Error [%]
Diameter[m]	8.0e-03	8.0e-03	0.
Length[m]	5.3e-03	5.3e-03	0.
Volume[m^3]	2.66407e-07	2.66413e-07	2.331e-03
Mass[kg]	3.1e-04	3.10007e-04	2.331e-03
Moment of	1.966e-09[a]	1.9674e-09[a]	7.543e-02
inertia [$kg.m^2$]	2.480e-09[b]	2.4793e-09[b]	2.626e-02
k_n ($N\ m^{-1}$)	10^5	10^5	—
e_n	0.85	0.85	—
μ_c	0	0	—
$\delta_{max}\ (m)$, δ_{max}/l_c	3.345×10^{-5} , 0.00263	3.345×10^{-5} , 0.00263	—
$T_C\ (s)$	1.14×10^{-4}	1.14×10^{-4}	—
$\Delta t\ (s)$	5×10^{-6}	5×10^{-6}	—

[a] about central diameter, [b] about central axis.

Table 1 Experimental [19] and numerical parameters for the normal impact of a cylinder on a flat wall. Contact force model parameters and estimate of contact features at $v_{col} = 1\,m/s$. l_c is the characteristic length of the object.

Parameter	Experiment	Glued-sphere model of [19]	Our glued-sphere model (True parameters)
Diameter[m]	8.0e-03	8.0e-03	8.0e-03
Length[m]	5.3e-03	5.3e-03	5.3e-03
Volume[m^3]	2.664e-07	1.916e-07(9 spheres)	1.948e-07(9 spheres)
	2.664e-07	2.231e-07(54 spheres)	2.244e-07(54 spheres)
Mass[kg]	3.1e-04	3.1e-04	2.266e-04(9 spheres)
			2.611e-04(54 spheres)
Moment of	1.966e-09[a]	1.966e-09[a]	1.320e-09[a](9 spheres)
inertia[$kg \cdot m^2$]	2.480e-09[b]	2.480e-09[b]	1.738e-09[b](9 spheres)
			1.830e-09[a](54 spheres)
			1.871e-09[b](54 spheres)
k_n ($N\,m^{-1}$)	10^5	10^5	10^5
e_n	0.85	0.85	0.85
μ_c	0	0	0
δ_{max} (m) , δ_{max}/l_c	3.345×10^{-5} , 0.00263	3.345×10^{-5} , 0.00263	3.345×10^{-5} , 0.00263
T_C (s)	1.14×10^{-4}	1.14×10^{-4}	1.14×10^{-4}
Δt (s)	5×10^{-6}	5×10^{-6}	5×10^{-6}

[a] about central diameter, [b] about central axis

Table 2 Experimental and numerical parameters for the normal impact of a cylinder modelled with glued spheres on a flat wall. Contact force model parameters and estimate of contact features at $v_{col} = 1\,m/s$. l_c is the characteristic length of the object.

Parameter	Value
Particle-Wall	
$k_n \ (N \, m^{-1})$	1×10^5
e_n	0.9
μ_c	0
$\delta_{max} \ (m) \, , \ \delta_{max}/l_c$	$2.04 \times 10^{-5} \, , \ 0.00816$
$T_C \ (s)$	3.15×10^{-5}
$\Delta t \ (s)$	2×10^{-6}

Table 3 Contact force model parameters, estimate of contact features at $v_{col} = 1 \, m/s$ and time step magnitude used for the normal impact of a cube on a flat wall. l_c is the characteristic length of the object.

Parameter	Value
Particle-Plexiglas	
k_n $(N\,m^{-1})$	1×10^5
e_n	0.5
μ_c	0.4
$\delta_{max}\,(m)$, δ_{max}/l_c	9.795×10^{-6} , 0.00489
T_C (s)	1.86×10^{-4}
Particle-Particle	
k_n $(N\,m^{-1})$	1×10^5
e_n	0.6
μ_c	0.4
$\delta_{max}\,(m)$, δ_{max}/l_c	9.795×10^{-6} , 0.0065
T_C (s)	1.33×10^{-4}
Particle-Plastic wall	
k_n $(N\,m^{-1})$	1×10^5
e_n	0.6
μ_c	0.6
$\delta_{max}\,(m)$, δ_{max}/l_c	9.795×10^{-6} , 0.00489
T_C (s)	1.86×10^{-4}
Δt (s)	7.5×10^{-6}

Table 4 Contact force model parameters, estimate of contact features at $v_{col} = 1\,m/s$ and time step magnitude used in the comparison of rotating drum simulation results against experimental data. l_c is the characteristic length of the object.

Shapes	Spheres	Cylinders	Cubes	Tetrahedron	2D cross	3D cross
ε	38.1772	38.5866	39.619	47.4582	69.4569	79.6328
Nb points*	3.2×10^7				6.4×10^7	
ε	38.1794	38.5811	39.5899	47.4586	69.4573	79.6327
Nb points*	2.56×10^8				5.12×10^8	

* Total number of cells in the structured mesh used to estimate ε

Table 5 Estimation of the porosity ε [%]. The domain is dicretised in the three direction.

Parameter	Value
k_n $(N\,m^{-1})$	1×10^5
e_n	0.73
μ_c	0.55
δ_{max} (m) , δ_{max}/R_e	1.1403×10^{-5} , 0.007602
T_C (s)	4.172×10^{-5}
Δt (s)	2×10^{-6}

Table 6 Contact force model parameters, estimate of contact features at $v_0 = 1\,m\,s^{-1}$ and time step magnitude used in numerical simulations of 2D/3D crosses in the rotating drum of [39].

List of Figures

Figure 1 2D illustration of the decomposition of a non-convex particle into a set of elementary convex components.

Figure 2 Discretisation strategy illustrated in 2D.

(a) Volume
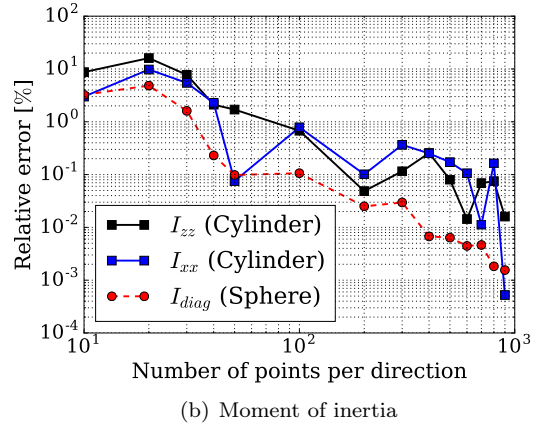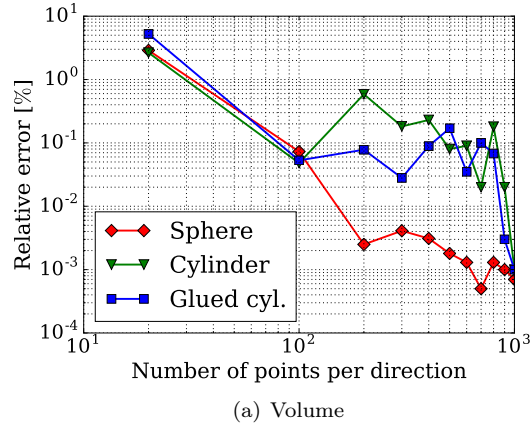
(b) Moment of inertia

Figure 3 Relative error on (a) the volume and (b) components of the moment of inertia tensor, of a sphere, a cylinder and a glued convex made of two overlapping cylinders, as a function of the number of discretization points per direction.
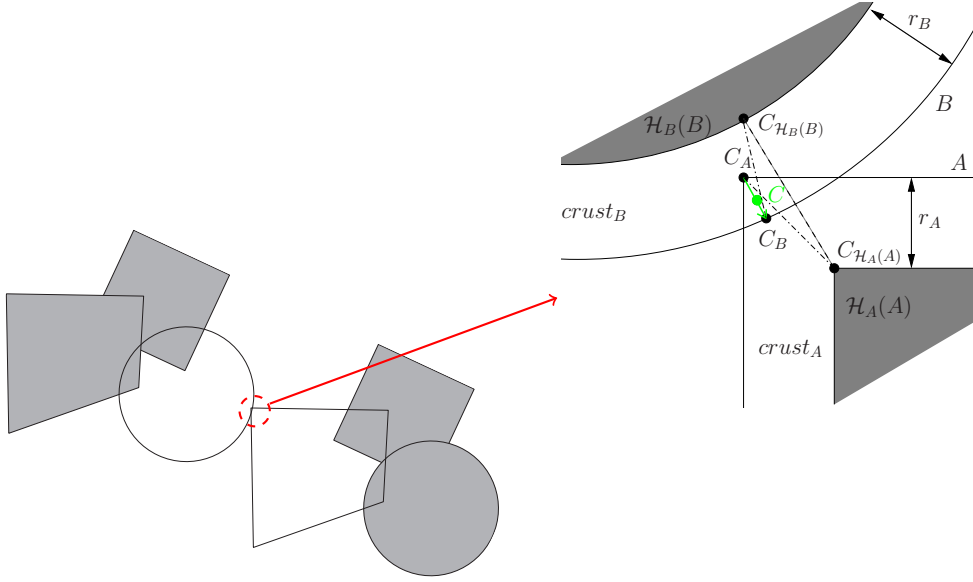
Figure 4 Contact between non-convex particles: contact occurs when at least one pair of convex elementary components are in contact.
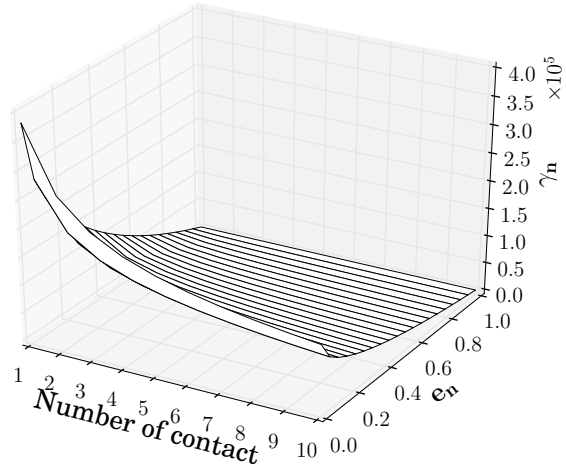
Figure 5 Dissipative normal coefficient γ_n as a function of restitution coefficient e_n and number of contact points N_c.
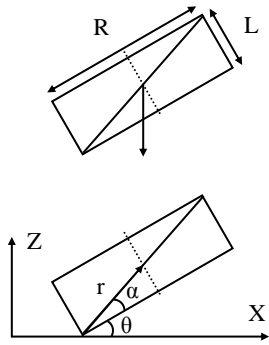
(a) Scketch of cylinder-wall impact. Credit: [19, 30].
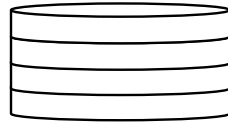
(b) A cylinder decomposed into thinner cylinders.
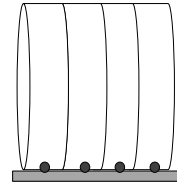
(c) Illustration of cylinder-wall impact at $90°$.

Figure 6 Sketch of the cylinder-wall impact test case.

(a) Translational velocity $V_{z,g}^+/V_{z,g}^-$.

(b) Angular velocity, $r\omega_y^+/V_{z,g}^-$.
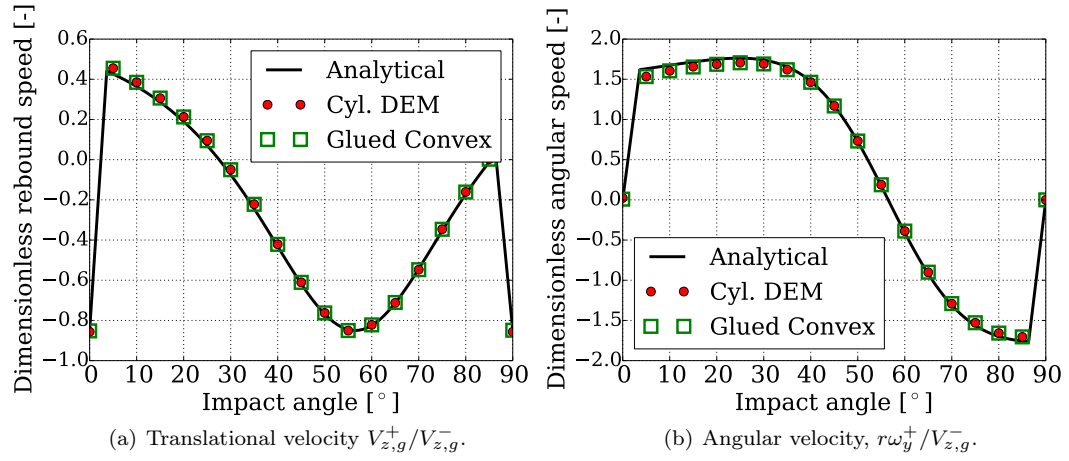
Figure 7 Cylinder-wall impact test case: comparison of the computed dimensionless post-impact velocities for the real cylinder and the *glued cylinder* to the analytical solution.
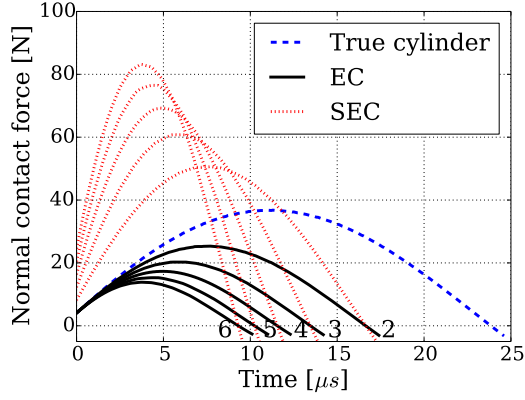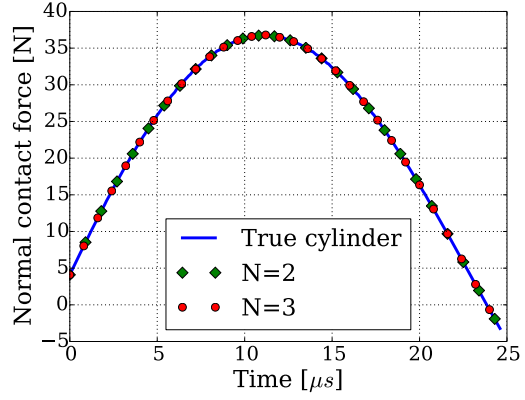
(a) Model A (b) Model B

Figure 8 Cylinder-wall impact test case at an angle of $90°$: normal contact force evolution with time. $N = 1, \ldots, 6$ is the number of elementary cylinders of the *glued cylinder*. EC denotes the normal force exerted on each elementary cylinder and SEC denotes the sum of the normal forces exerted on each elementary cylinder, i.e., the sum of the ECs.

(a) Relative error on $V_{z,g}^+$.

(b) Angular speed $\|\omega_y^+\|$ at 90°.
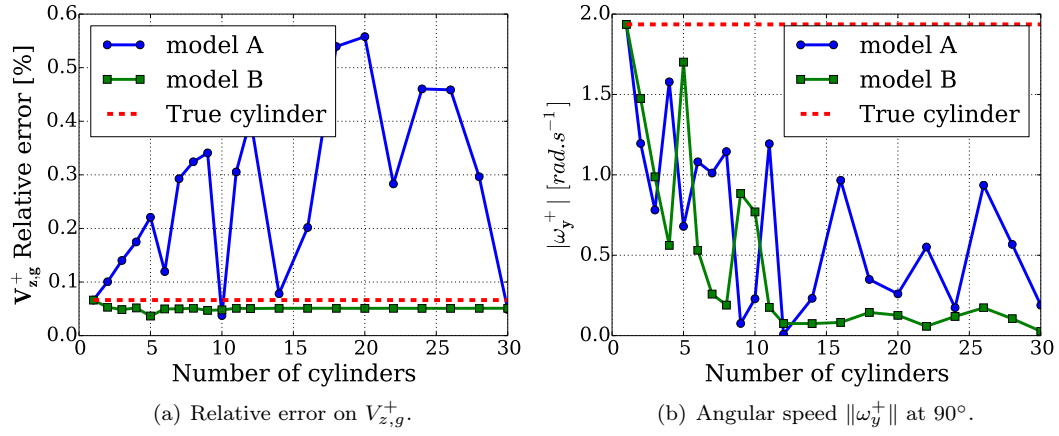
Figure 9 Cylinder-wall impact test case at an angle of 90°: error on post-impact velocities to the analytical solution for a true cylinder and for the 2 models as a function of the number of elementary cylinders of the *glued cylinder*.
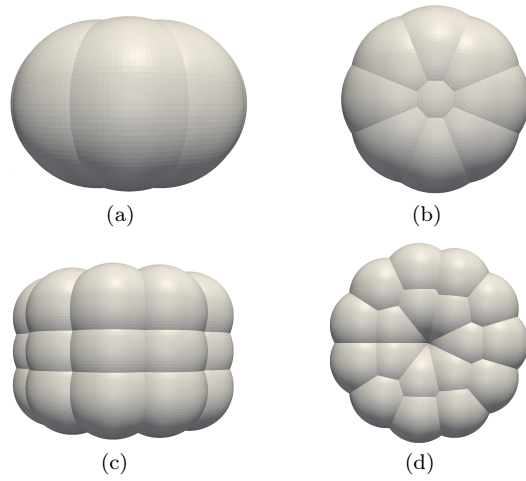
Figure 10 Cylinder-wall impact test case: glued-sphere approximations of the cylinder considered: (a)-(b) made of 9 glued spheres, (c)-(d) made of 54 glued spheres.

(a) Translational velocity $V_{z,g}^+/V_{z,g}^-$.

(b) Angular velocity $r\omega_y^+/V_{z,g}^-$.

(c) Translational velocity $V_{z,g}^+/V_{z,g}^-$.

(d) Angular velocity $r\omega_y^+/V_{z,g}^-$.
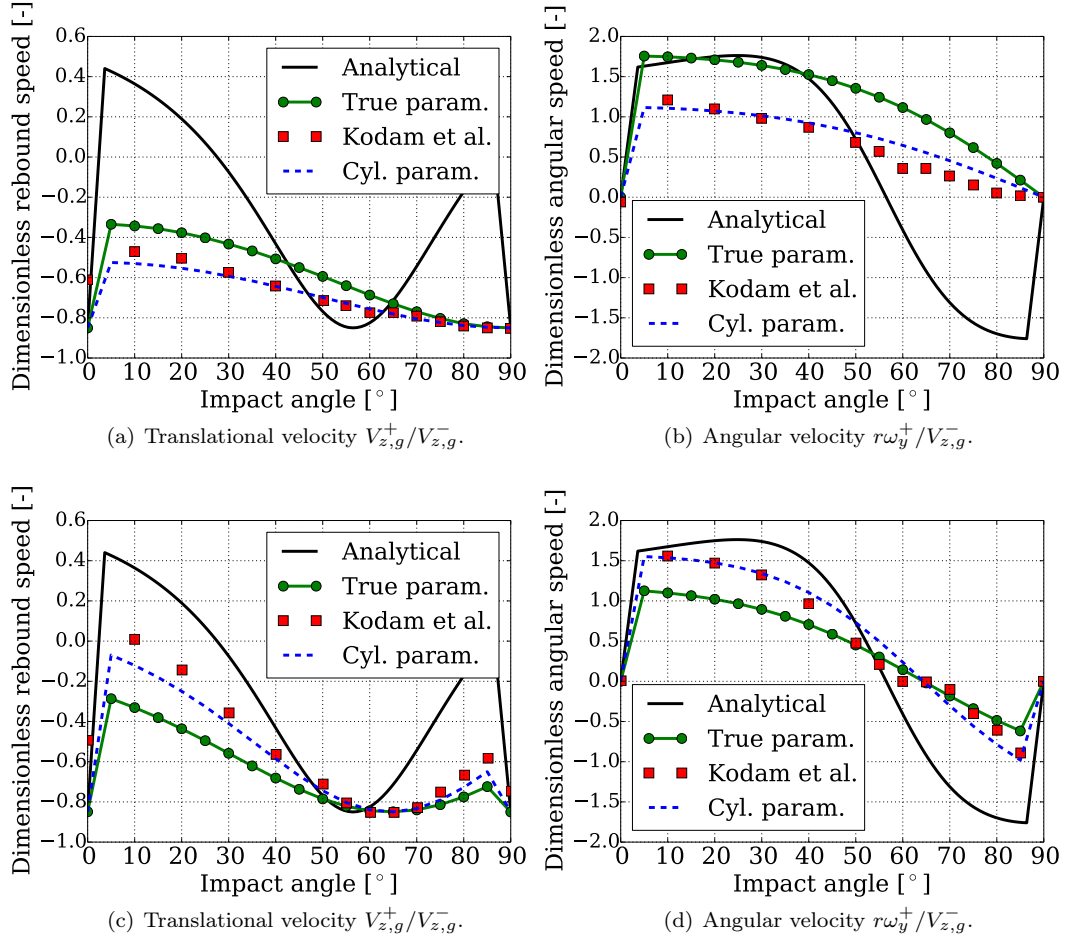
Figure 11 Cylinder-wall impact test case: comparison of the computed dimensionless post-impact velocities (a,b) for the 9 glued-sphere cylinder, and (c,d) for 54 glued sphere cylinder with the analytical solution.
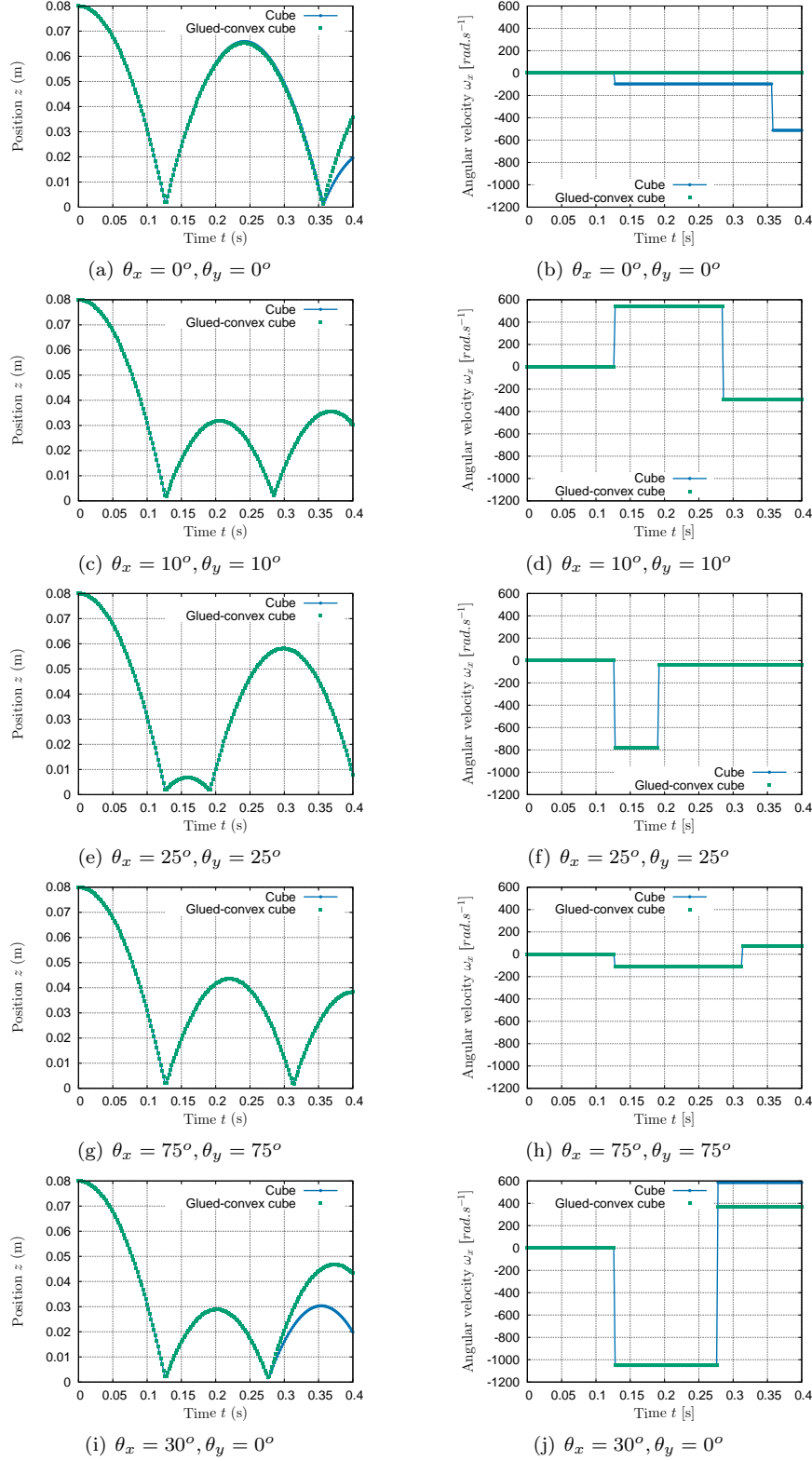
Figure 12 Cube-wall impact test case: comparison of vertical position time evolution and x-component of angular velocity time evolution for a single cube and a glued convex cube obtained by gluing 8 smaller cubes of half the edge length of the single cube released with various initial angular position $(\theta_x, \theta_y) = (0^o, 0^o)$, $(10^o, 10^o)$, $(25^o, 25^o)$, $(75^o, 75^o)$ and $(30^o, 0^o)$.
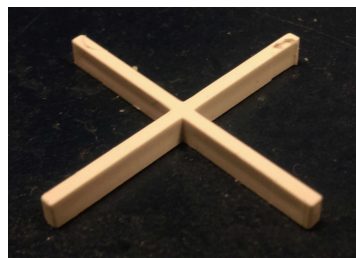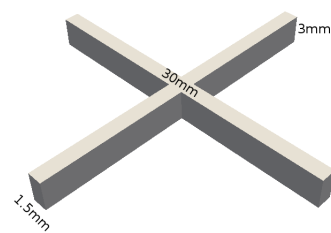
(a) Real shape   (b) DEM shape

Figure 13 Tile spacers used in experiments.

(a) Experimental set-up
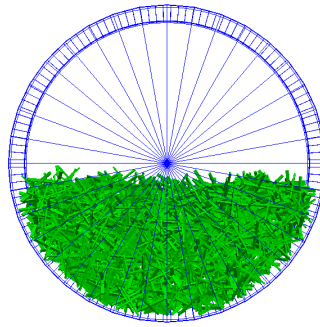
(b) Simulation set-up

Figure 14 Tile spacers experiments.
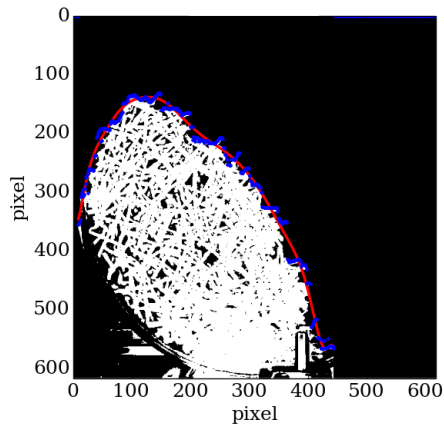
(a) Experimental image
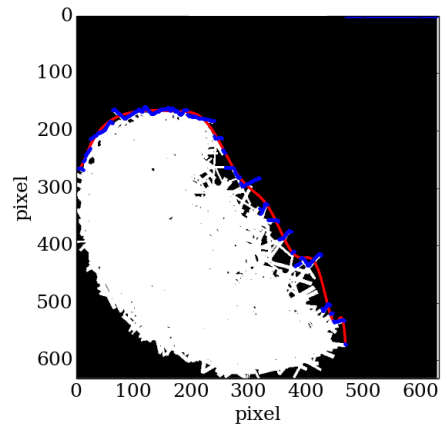
(b) DEM simulation image

Figure 15 Tile spacers experiments: method to identify the free surface of the granular media. The blue dots depict the free surface and the red line the polynomial fitting function of high order.
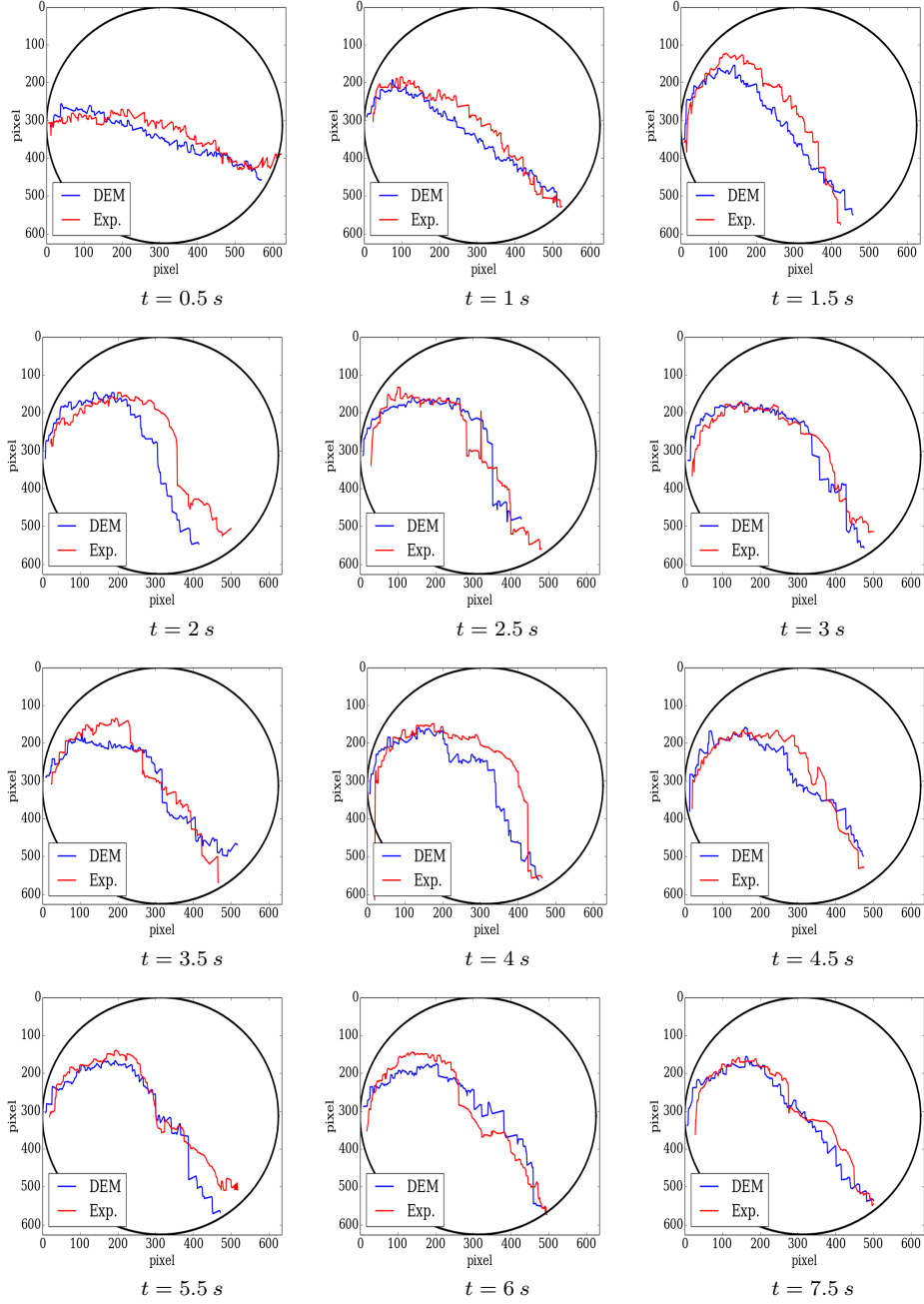
Figure 16 Tile spacers experiments: comparison of the free surface between numerical simulation and experiment data.
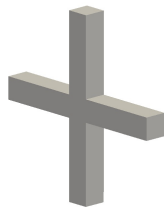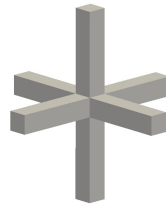
(a) 2D cross shape   (b) 3D cross shape

Figure 17 Non-convex cross-like shapes considered in the packing test case.

(a) Spheres

(b) Cylinders

(c) Cubes

(d) Tetrahedron

(e) 2D cross

(f) 3D cross
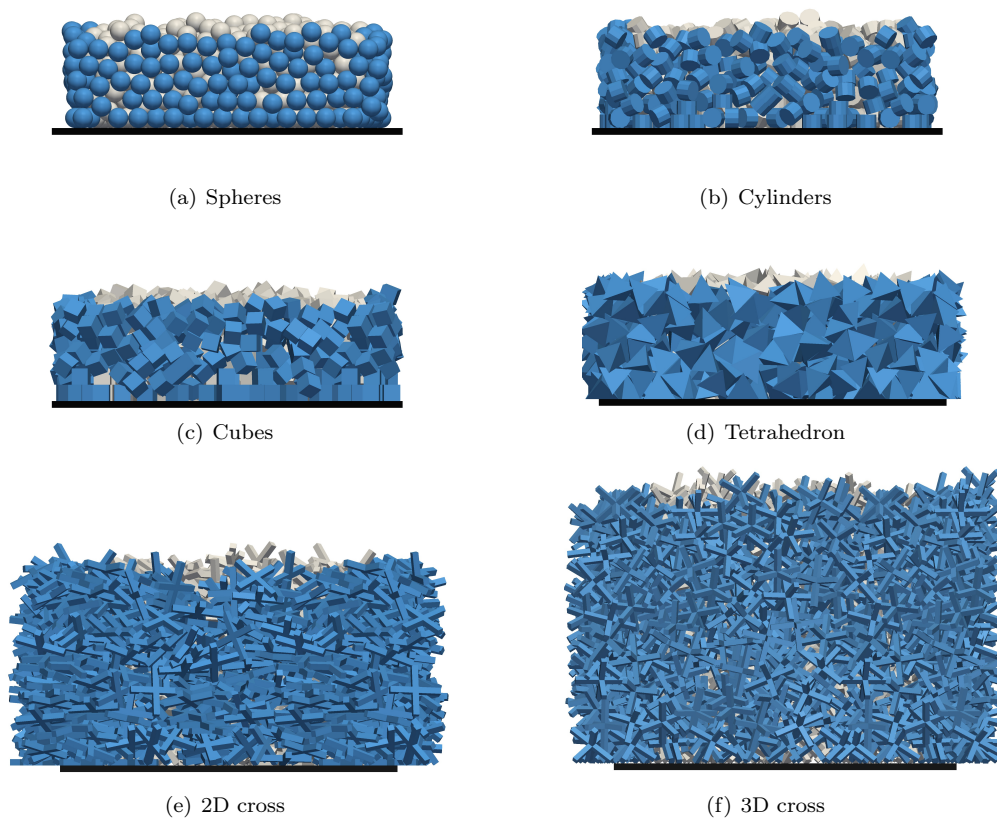
Figure 18 Packings of 1000 particles of 6 different shapes. Particles in blue are the periodic clones.

(a) Sphere   (b) Cylinder   (c) Cube   (d) Tetrahedron   (e) 2D-cross   (f) 3D-cross
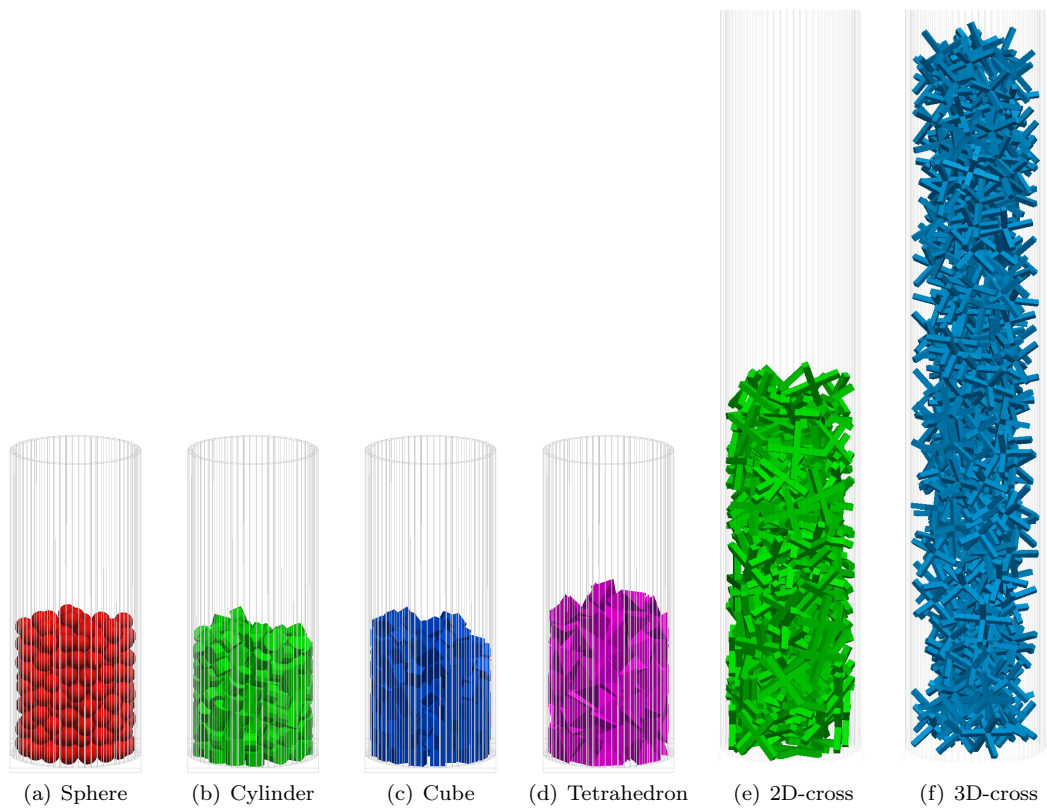
Figure 19 Packing of 250 particles of 6 different shapes in a cylindrical container. Results in (a,b,c,d) are from [39].

(a) $\Omega = 5\,rpm$

avalanching regime

(b) $\Omega = 20\,rpm$

avalanching regime

(c) $\Omega = 80\,rpm$

avalanching regime

(d) $\Omega = 125\,rpm$

cataracting regime

(e) $\Omega = 150\,rpm$

pseudo-cataracting regime

(f) $\Omega = 200\,rpm$

centrifuging regime
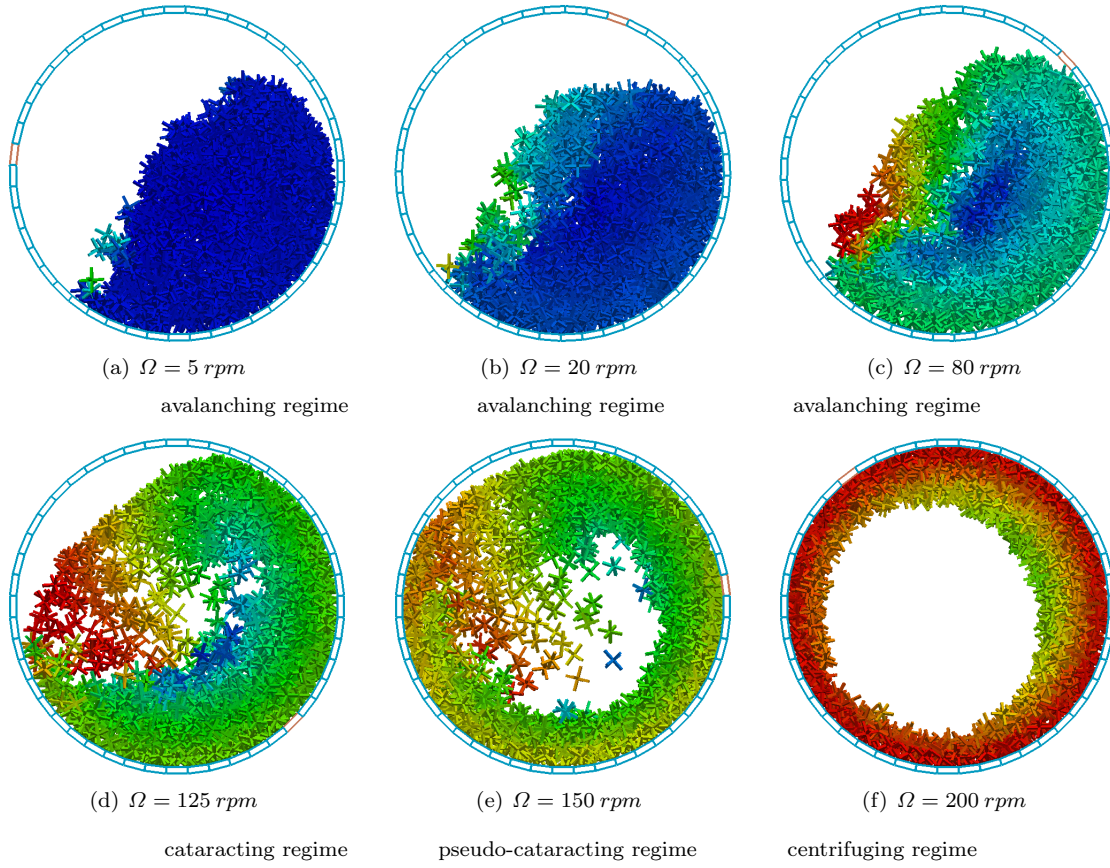
Figure 20 Rotating drum filled with 3D crosses at various rotation rates: snapshots of the pattern of particles colored by their translational velocity magnitude (from blue (min) to red (max)).

(a) Sphere
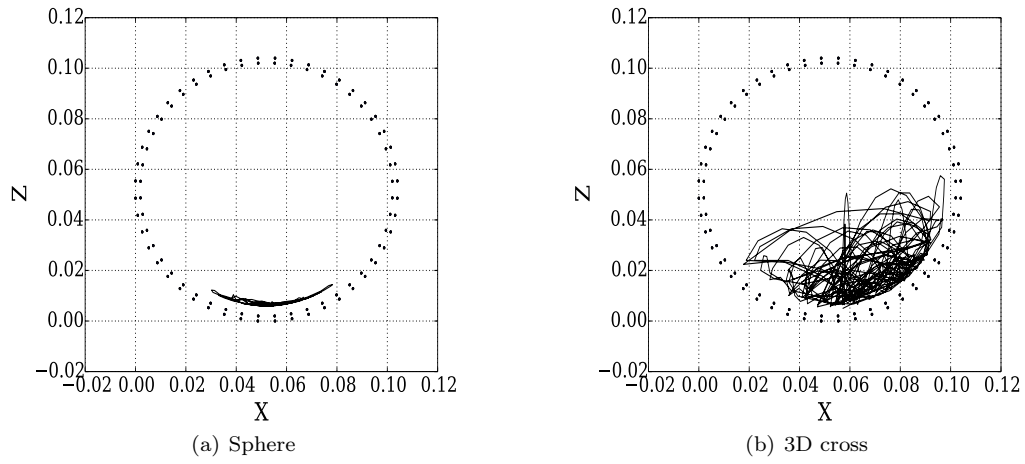
(b) 3D cross

Figure 21 Trajectory of a single particle at $\Omega = 150\,rpm$ over $10\,s$.

(a) $t = 4.05\ s$ (b) $t = 4.225\ s$ (c) $t = 4.35\ s$

(d) $t = 6\ s$ (e) $t = 6.1\ s$ (f) $t = 6.25\ s$
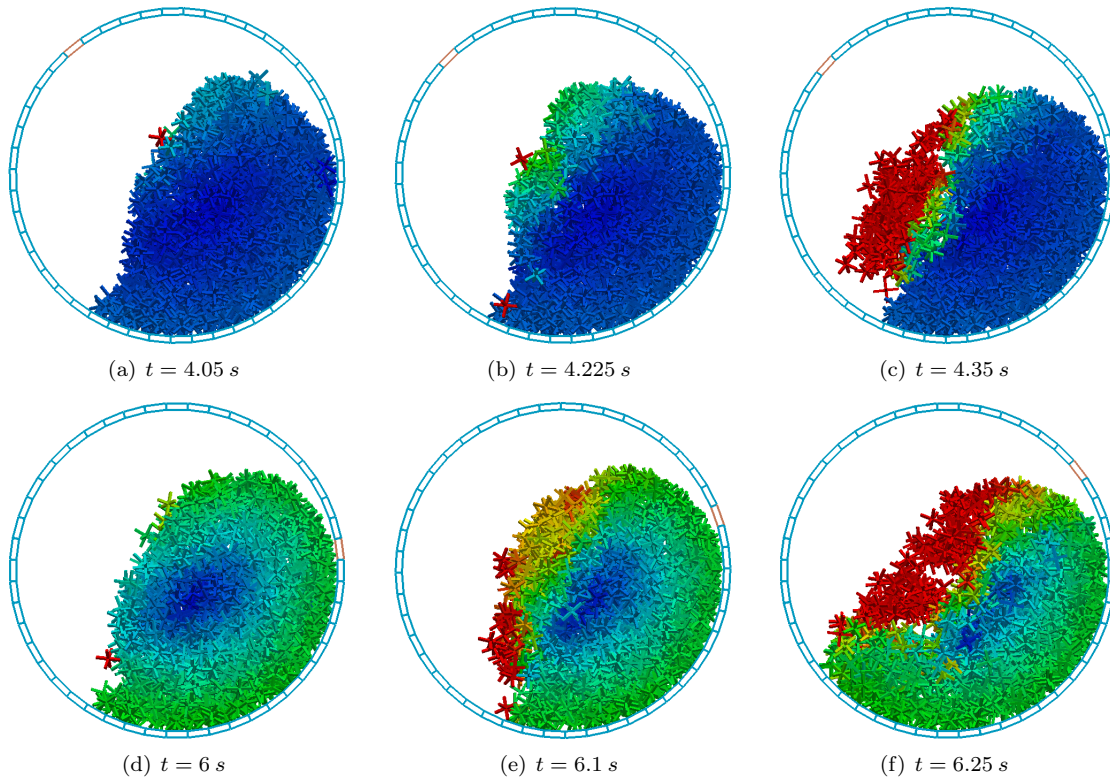
Figure 22 Avalanching regime of 3D crosses (a,b,c) at $\Omega = 5\ rpm$ and (d,e,f) at $\Omega = 20\ rpm$. Snapshots of the pattern of particles colored by their translational velocity magnitude (from blue (min) to red (max)) selected at 3 close times to evidence the occurence of an avalanche.
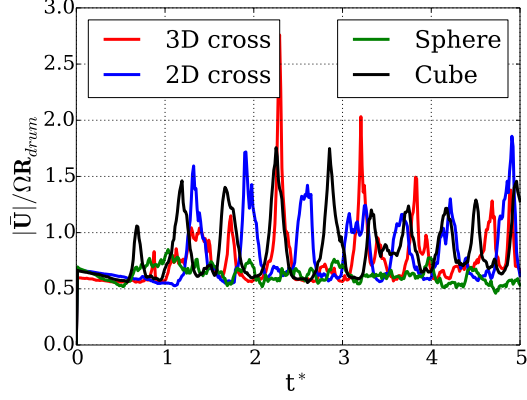
(a) $\Omega = 5\,rpm$

avalanching regime

(b) $\Omega = 20\,rpm$

avalanching regime

(c) $\Omega = 80\,rpm$

avalanching regime

(d) $\Omega = 125\,rpm$

cataracting regime

(e) $\Omega = 150\,rpm$

pseudo-cataracting regime

(f) $\Omega = 200\,rpm$

centrifuging regime
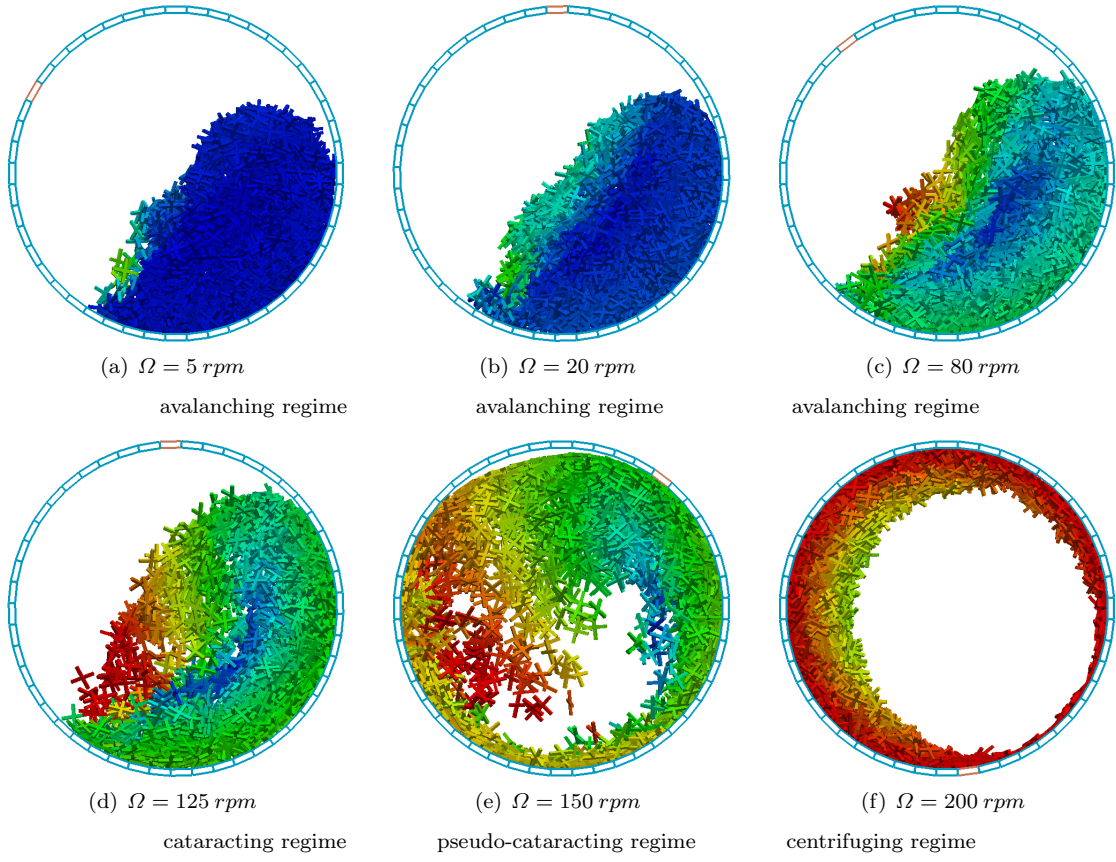
Figure 23 Rotating drum filled with 2D crosses at various rotation rates: snapshots of the pattern of particles colored by their translational velocity magnitude (from blue (min) to red (max)).

(a) $t = 8.9\,s$ (b) $t = 9\,s$ (c) $t = 9.2\,s$
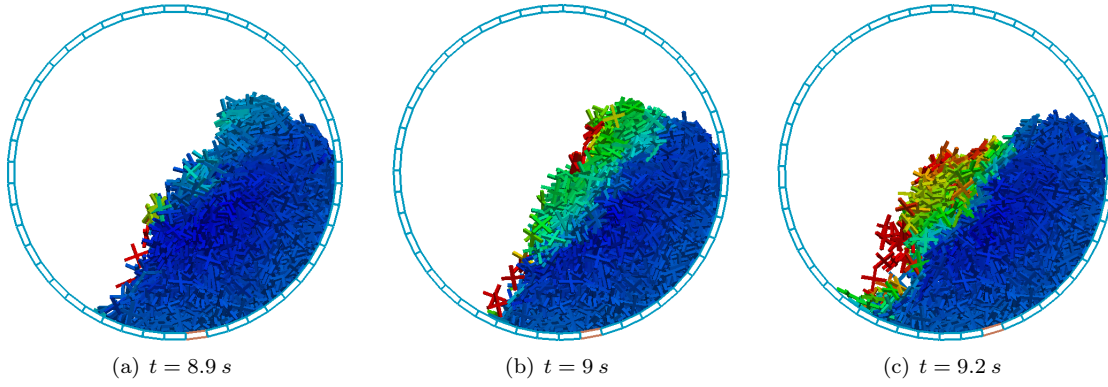
Figure 24 Avalanching regime of 2D crosses at $\Omega = 5\,rpm$. Snapshots of the pattern of particles colored by their translational velocity magnitude (from blue (min) to red (max)) selected at 3 close times to evidence the occurence of an avalanche.
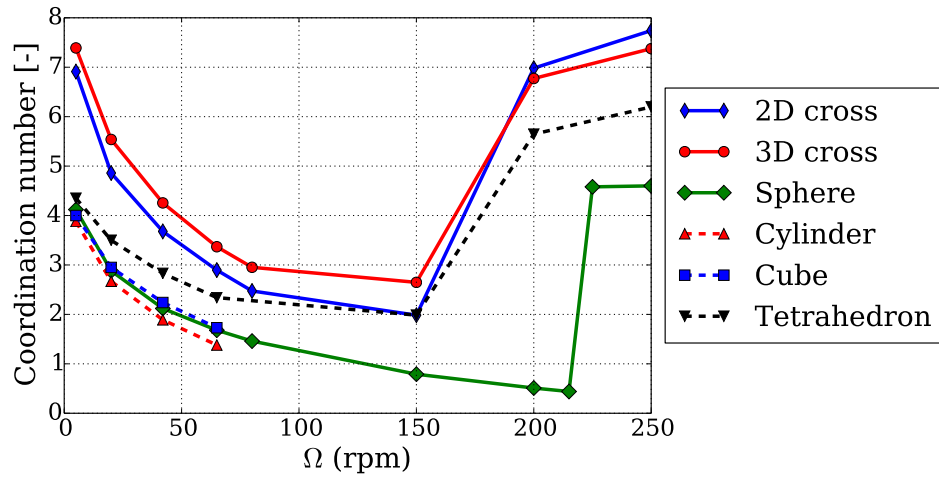
Figure 25 Time averaged coordination number as a function of rotation rate for all particle shapes considered. Data for spheres, cylinders, cubes and tetrahedra are from [39]
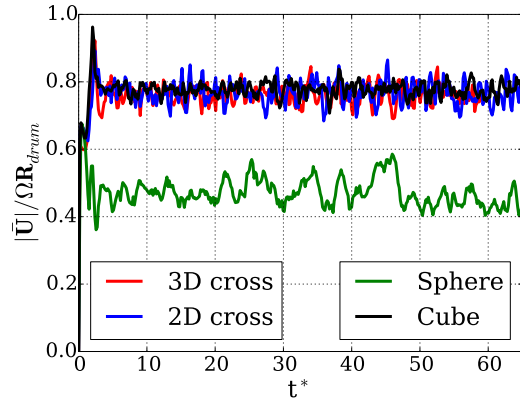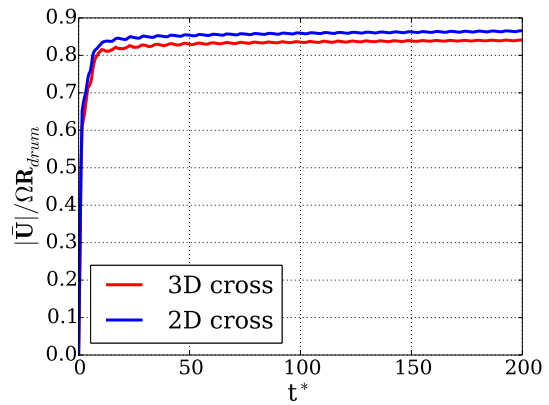
(a) $\Omega = 5\,rpm$
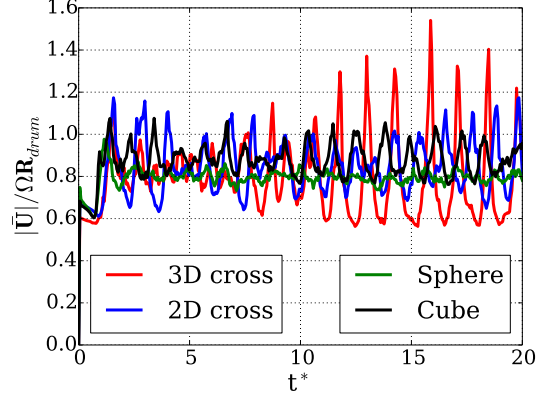
(b) $\Omega = 20\,rpm$
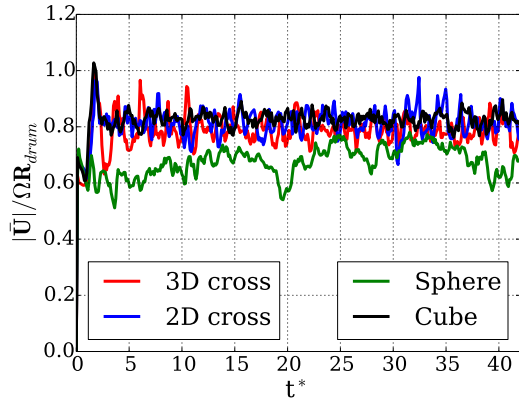
(c) $\Omega = 42\,rpm$

(d) $\Omega = 65\,rpm$
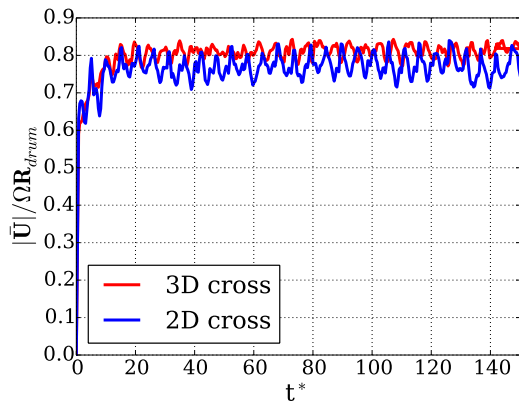
(e) $\Omega = 150\,rpm$

(f) $\Omega = 200\,rpm$

Figure 26 Evolution of dimensionless mean particle translational velocity as a function of dimensionless time $t^* = t\Omega$. Data for spheres and cubes are from [39].
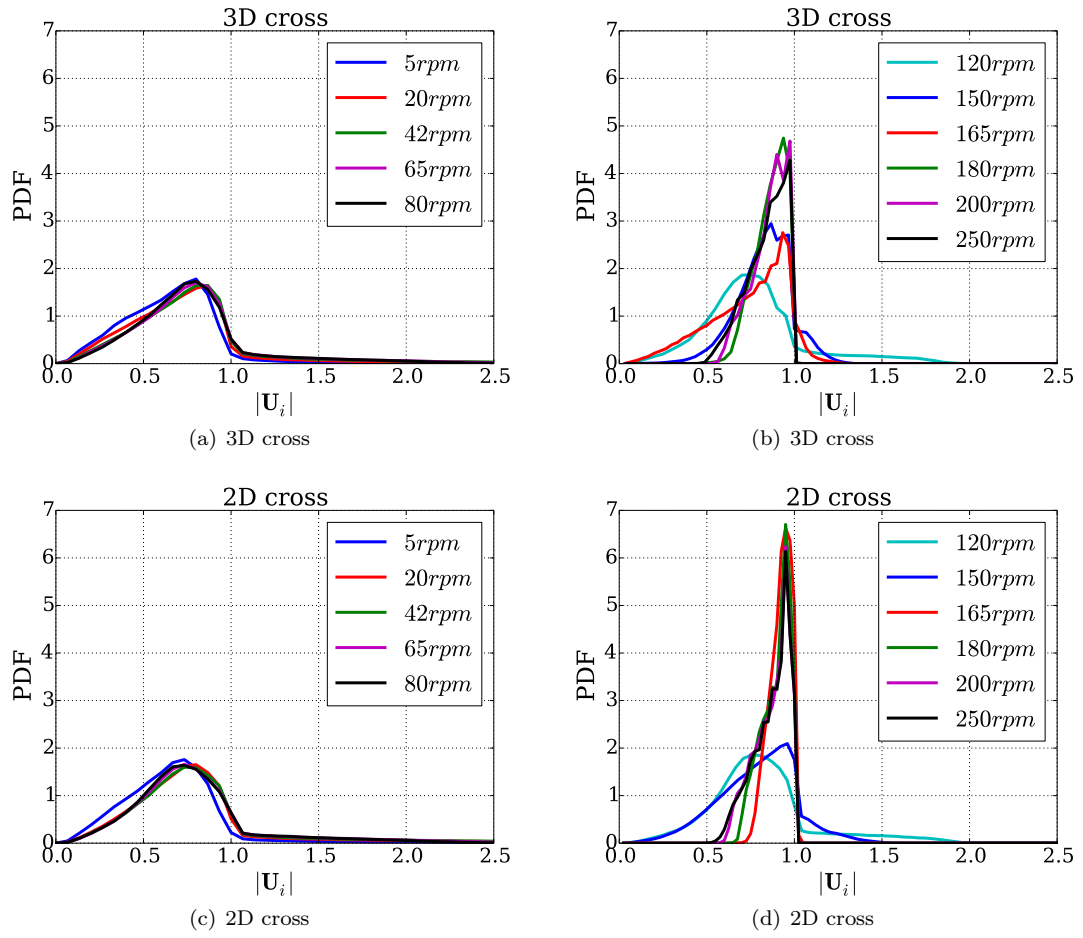
Figure 27 Probability density function of the time averaged particle translational velocity.
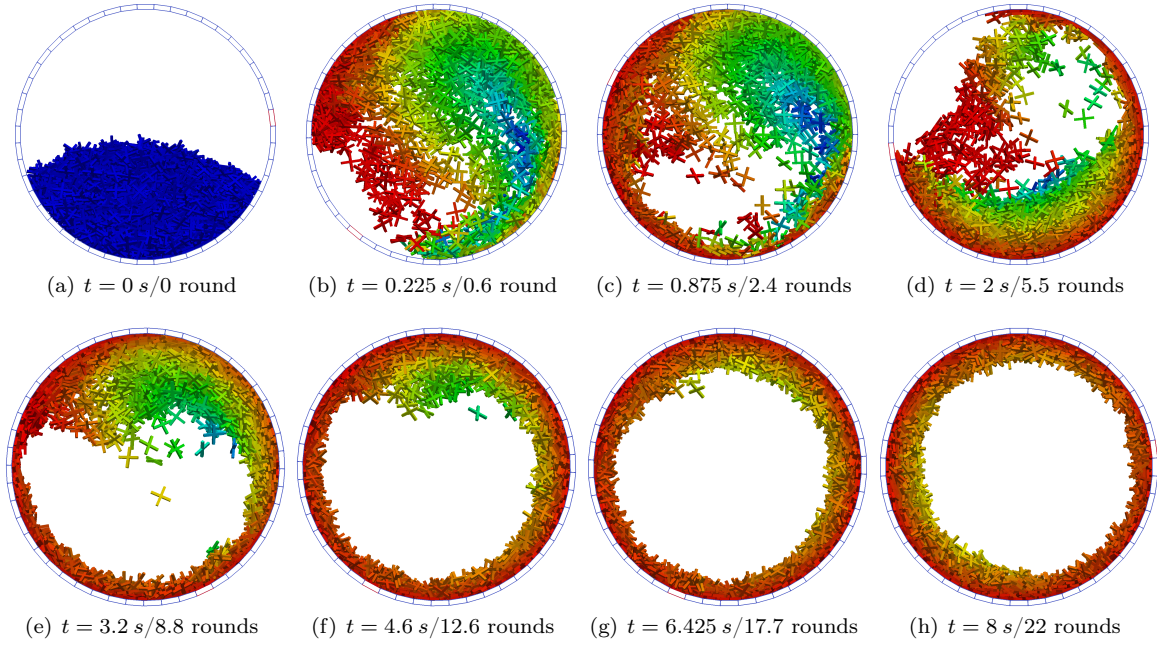
(a) $t = 0 \, s/0$ round   (b) $t = 0.225 \, s/0.6$ round   (c) $t = 0.875 \, s/2.4$ rounds   (d) $t = 2 \, s/5.5$ rounds

(e) $t = 3.2 \, s/8.8$ rounds   (f) $t = 4.6 \, s/12.6$ rounds   (g) $t = 6.425 \, s/17.7$ rounds   (h) $t = 8 \, s/22$ rounds

Figure 28 Transient regime of 2D crosses at $\Omega = 165 \, rpm$ from $t = 0s$ to $t = 8s$ (22 rounds). Snapshots of the pattern of particles colored by their translational velocity magnitude (from blue (min) to red (max)) at selected times. Centrifuging regime is eventually established after about 20 rounds.
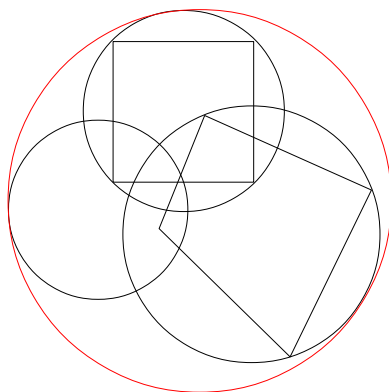
Figure 29 Sphere circumscribed to a non-convex particle with spheres circumscribed to its elementary convex components illustrated in 2D.
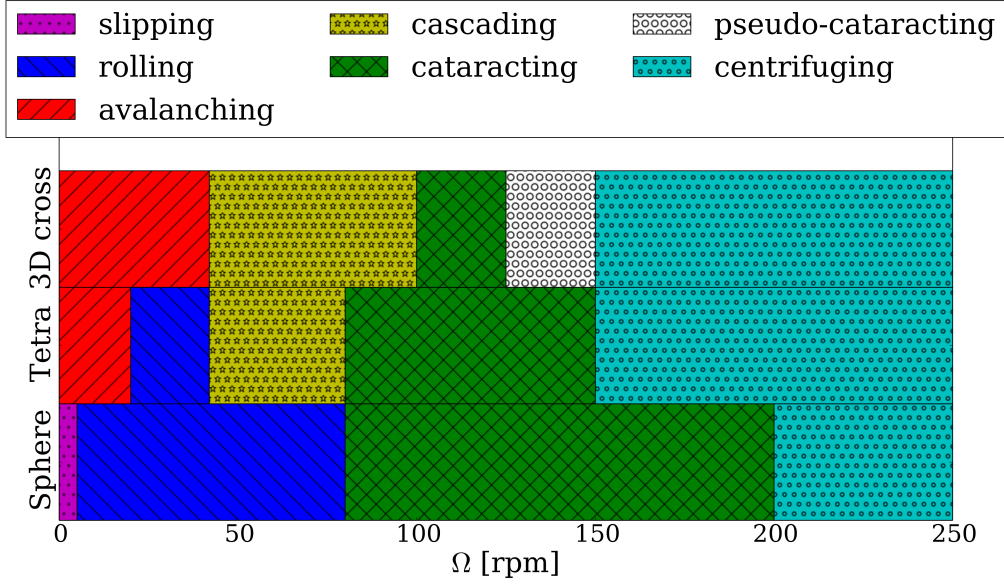
Figure 30 Rotating drum flow regime map as a function of rotation rate and particle shape.